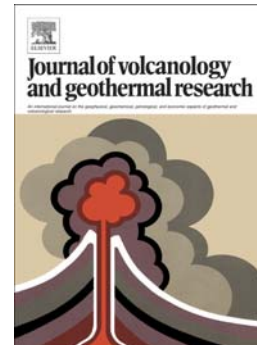# Accepted Manuscript

Inter-comparison of three-dimensional models of volcanic plumes

Y.J. Suzuki, A. Costa, M. Cerminara, T. Esposti Ongaro, M. Herzog, A.R. Van Eaton, L.C. Denby

Inter-comparison of three-dimensional models of volcanic plumes

Y. J. Suzuki (1), A. Costa (1,2), M. Cerminara (3), T. Esposti Ongaro (3),

M. Herzog (4), A. R. Van Eaton (5), L.C. Denby (4)

1- Earthquake Research Institute, The University of Tokyo, Japan

2- Istituto Nazionale di Geofisica e Vulcanologia, Bologna, Italy

3- Istituto Nazionale di Geofisica e Vulcanologia, Pisa, Italy

4- Department of Geography, University of Cambridge, UK

5- U.S. Geological Survey Cascades Volcano Observatory, Vancouver, WA, USA

Abstract

We performed an inter-comparison study of three-dimensional models of volcanic plumes. A set of common volcanological input parameters and meteorological conditions were provided for two kinds of eruptions, representing a weak and a strong eruption column. From the different models, we compared the maximum plume height, neutral buoyancy level (where plume density equals that of the atmosphere), and level of maximum radial spreading of the umbrella cloud. We also compared the vertical profiles of eruption column properties, integrated across cross-sections of the plume (integral variables). Although the models use different numerical procedures and treatments of subgrid turbulence and particle dynamics, the inter-comparison shows qualitatively consistent results. In the weak plume case (mass eruption rate 1.5×10^6 kg s^{-1}), the vertical profiles of plume properties (e.g., vertical velocity, temperature) are similar among models, especially in the buoyant plume region. Variability among the simulated maximum heights is ~20%, whereas neutral

buoyancy level and level of maximum radial spreading vary by ~10 %. Time-averaging of the three-dimensional (3D) flow fields indicates an effective entrainment coefficient around 0.1 in the buoyant plume region, with much lower values in the jet region, which is consistent with findings of small-scale laboratory experiments. On the other hand, the strong plume case (mass eruption rate 1.5×10^9 kg s^{-1}) shows greater variability in the vertical plume profiles predicted by the different models. Our analysis suggests that the unstable flow dynamics in the strong plume enhances differences in the formulation and numerical solution of the models. This is especially evident in the overshooting top of the plume, which extends a significant portion (~1/8) of the maximum plume height. Nonetheless, overall variability in the spreading level and neutral buoyancy level is ~20 %, whereas that of maximum height is ~10%. This inter-comparison study has highlighted the different capabilities of 3D volcanic plume models, and identified key features of weak and strong plumes, including the roles of jet stability, entrainment efficiency, and particle non-equilibrium, which deserve future investigation in field, laboratory, and numerical studies.

1. Introduction

Understanding the dynamics of eruption columns during explosive eruptions is one of the central aims of volcanology. In particular, improving the relationships between plume height, vertical distribution of mass, and initial eruptive conditions is crucial to improve forecasts of atmospheric ash dispersal. The maximum height of a volcanic plume is commonly used to estimate its mass eruption rate and vertical distribution of mass (Suzuki, 1983; Sparks et al., 1997; Mastin et al., 2009; Folch, 2012). However, many factors can lead eruption plumes to deviate from these simple empirical relationships (e.g., Tupper et al., 2009). Therefore, it is important to develop a clearer understanding of the behaviour of three-dimensional volcanic plumes under different meteorological and eruptive conditions.

Over the past few decades, a range of numerical models have been developed to examine the dynamics of eruption columns (Costa et al., 2016). In this work we specifically address fluid dynamic models of volcanic plumes which solve the full Eulerian transient mass, momentum, and energy equations for the plume mixture and ambient air in a three-dimensional atmospheric domain. With respect to one-dimensional (1D) integral models discussed in the companion paper (Costa et al., 2016), three-dimensional (3D) models can describe the non-homogeneous features of a volcanic plume, i.e., the time- and space-dependent distribution of the concentration, temperature, pressure, and velocity of each constituent of the eruptive mixture, and the multiphase flow features of the eruptive mixture. In addition, they can explicitly simulate turbulent entrainment of ambient air by resolving the eddy structure of the plume and the stratification and flow circulation in the atmosphere. Although 3D models were developed for volcanological applications in the 1990s (Valentine and Wohletz, 1989; Dobran et al., 1993; Oberhuber et al., 1998), only in the last decade

3D simulations have become computationally affordable thanks to the advent of high-performance computing (e.g., Suzuki et al., 2005; Textor et al., 2005; Esposti Ongaro et al., 2008; Herzog et al., 2010; Van Eaton et al., 2015; Cerminara et al., 2016a).

In this study, 3D results are used to enhance our understanding of the processes occurring inside volcanic plumes and, in particular, to investigate their non-homogeneous structure. Plume dynamics are mainly analysed on their time- and space-averaged properties to allow comparison with 1D integral models and discuss their approximations and the capability to capture some features especially relevant for volcanic hazard assessment, such as the maximum plume height and the level of spreading of the umbrella. However, plume average properties are controlled by turbulent fluctuations, occurring on small time and space scales (for a discussion of turbulent scales see, e.g., Cerminara et al., 2016a). These are explicitly resolved in 3D models while they are parameterized in integral models by means of an empirical entrainment coefficient (Morton et al., 1956). Therefore, comparison of 1D and 3D models can allow the improvement the parameterization of entrainment in 1D models (Suzuki and Koyaguchi, 2012; Cerminara et al., 2016b).

This work is a part of a more general inter-comparison study of eruption column models promoted by the IAVCEI Commission on Tephra Hazard Modelling, in which a set of simulations were performed by both 3D models and 1D integral models (Costa et al., 2016). In the present study, we describe the 3D models and discuss their discrepancies and similarities on the basis of the assumptions and approximations made in each modelling approach. Finally, we discuss the method for comparing and analysing 3D simulation results and the implications for modelling volcanic plumes under different meteorological and eruptive conditions.

2. Methods

For this study, 3D numerical simulations were performed with four different models, using the same volcanic and meteorological conditions. Each 3D model is based on the time-dependent solution of the generalized multiphase flow Navier-Stokes equations for conservation of mass, momentum, and energy (or enthalpy), describing the fluid dynamics of the eruptive mixture and the surrounding atmosphere, the thermodynamic equation of state, and the constitutive equations. The key differences between the models are the treatments of the gas-particle mixture, water microphysics and subgrid turbulence. The numerical discretization and solution methods also differ. However, the aim of this inter-comparison (as in Costa et al., 2016) is to compare results with common input parameters, without constraining every aspect of the modelling (e.g., grid resolution, numerical discretization). This approach allows us to evaluate the results of different models as typically employed by the users.

In the following sections, we provide a brief description of each model and the common input parameters used for the inter-comparison. We then describe the specific methods used to quantitatively compare results from 3D models, and then, 1D models.

2.1 Physical formulations

These models describe the injection of a mixture of solid pyroclasts and volcanic gases from a vent into the stratified atmosphere. This inter-comparison study involves four different codes: SK-3D (Suzuki et al., 2005; Suzuki and Koyaguchi, 2009, 2013, 2015), ATHAM (Active Tracer High-resolution Atmospheric Model; Herzog et al., 1998; Van Eaton et al., 2012, 2015), ASHEE (Ash Equilibrium Eulerian

model; Cerminara et al., 2016a), and PDAC (Pyroclastic Dispersal Analysis Code; Neri et al., 2003; Esposti Ongaro et al., 2007; Carcano et al. 2013). In the present application, SK-3D, ATHAM, and PDAC considered eruption from a circular vent with steady mass flux. In ASHEE, a periodical forcing and a random perturbation of intensity $0.05U$ (U being the average flow velocity) has been superimposed to the average inflow to mimic a turbulent inlet at the vent and to trigger fluid instabilities. Such a perturbation has an important role in the jet region, where it significantly anticipates the development of turbulence (Cerminara et al., 2016a, 2016b). The main features of each model are summarized in Table 1 and briefly stated hereafter.

SK-3D employs a pseudo-gas or dusty-gas approximation in which the velocity and temperature are same for all phases (e.g., Marble, 1970). This approximation is also adopted by the 1D models analyzed in the model inter-comparison of Costa et al. (2016), and is physically justified for dilute plumes (volumetric particle concentration < 0.001; Elghobashi, 1991; 1994) containing small particles. Under this approximation, the mixture of solid particles and gas is treated as a single fluid, and particle-gas decoupling is ignored (Suzuki et al., 2005). As a result, SK-3D involves two components: eruptive material (the mixture of solid particles and water vapor) plus dry air.

ATHAM also assumes perfect coupling between particles and the flow in the horizontal direction, but does allow gravitational settling and separation of particles in the vertical direction. ATHAM considers cloud microphysical processes, including the phase changes of water vapor, liquid water, and ice, growth of precipitation (raindrops, hail), and the dynamic effects of latent heat exchange.

ASHEE uses the equilibrium-Eulerian approach (Ferry and Balachandar, 2001), which extends the applicability of the dusty gas model to coarser particles (from St <

10^{-3} to St < 0.2, where St is Stokes number; Balachandar and Eaton, 2010; Cerminara et al., 2016a). For volcanic plumes, such a threshold corresponds to ash particles (diameter less than about 1 mm). By using such an approach, the model can describe, to a first order, the kinematic decoupling of particles due to both settling and turbulence.

PDAC can model both the kinetic and thermal non-equilibrium interaction and decoupling between solid particles and gas by adopting an N-phase multicomponent Eulerian description (Neri et al., 2003; Esposti Ongaro et al., 2007; Esposti Ongaro and Cerminara, 2016). In such a description, the gas and particulate phases in the plume can have different velocities and temperatures, because of different injection regimes or because they are subject to different forces (such as the effective gravity, or buoyancy), while drag forces and heat exchange will tend to homogenize the flow.

2.2 Numerical procedures

Numerical procedures also differ among the models. The partial differential equations are solved numerically using a finite difference method in ATHAM and SK-3D, and a finite volume method in ASHEE and PDAC.

SK-3D uses the Roe scheme (Roe, 1981) with MUSCL (Monotone Upstream-centred Scheme for Conservation Laws) interpolation (van Leer, 1977) for spatial integration and the time splitting method for time integration. In ATHAM, transport is formulated in flux form to conserve mass and momentum. To avoid over- and undershoots in the solution, a correction term is added analogous to Smolarkiewicz (1984). The time integration follows a generalized Crank-Nicholson scheme (Crank and Nicholson, 1947) with a forward weight of 0.25. ASHEE is based on the open-source OpenFOAM code (www.openfoam.org). In this application, an unlimited, centred linear scheme (second order-accurate) and a Crank-Nicholson time-

integration scheme are used. The PISO-PIMPLE (Pressure Implicit with Splitting of Operators; Issa, 1986) semi-implicit solution procedure based on a pressure correction algorithm is used to resolve the algebraic system of discretized equations, conserving mass, momentum and energy in both low and high Mach number conditions. In PDAC the equations are solved by a semi-implicit second-order finite-volume discretization scheme (based on the limited MUSCL reconstruction) and a pressure-based iterative non-linear solver designed for compressible multiphase flows.

To simulate the dynamics of eruption columns, it is essential to correctly reproduce turbulent mixing. Large eddy simulation (LES) approach is used to describe subgrid-scale turbulence in ATHAM (Oberhuber et al., 1988), ASHEE (Moin et al., 1991), and PDAC (Smagorinsky, 1963). In contrast, SK-3D does not use the LES approach (Suzuki et al., 2005). In fact, according to the numerical work by Suzuki et al. (2005) which indicated that, when spatial resolution is sufficiently high (horizontal grid size smaller than ~D_0/20 at the vent, D_0 being the inlet diameter), both the numerical results with and without the LES model correctly reproduce the spreading rate of jets observed in the experiments. In such conditions, subgrid-scale models plays only a secondary role in reproducing the global features of turbulent mixing and the efficiency of entrainment.

The spatial resolution and numerical accuracy are essential to simulate turbulent structures and entrainment efficiency. In all models, numerical calculations are performed on a non-uniform (vertically and horizontally stretched) grid, with different grid resolutions and domain sizes. In SK-3D, the grid resolution is smaller than D_0/20 at the vent, increasing with distance from vent at a constant rate (by a factor of 1.02 for vertical and horizontal coordinates) up to D_0/2 for the weak plume, and up to 300 m for the strong plume. ATHAM uses a maximum resolution of D_0/3 for the weak

plume and $D_0/13$ for the strong plume near the vent, increasing to approximately 600 m (weak plume) and 4 km (strong plume) over domain widths of 50 km and 350 km for the weak and strong plumes, respectively. In ASHEE, the grid is cylindrical and it is specifically designed to keep the aspect ratio of the cells near to one (cf. Cerminara, 2016; Cerminara et al., 2016a, 2016b) with the resolution of $D_0/32$ at the vent, increasing constantly up to 70 m for the weak plume and 300 m for the strong plume. PDAC uses a Cartesian grid, with minimum resolution of $D_0/3$ for the weak plume and $D_0/30$ for the strong plume. Vertical grid size as a function of the vertical position for all the models is given in Appendix A. For simulations with a background wind, the vent location is off-center to allow for a larger model domain on the downwind side of the volcano. The spatial domain and the main computational parameters are reported, for each model, in Table 2. It is worth remarking that the adopted time-step is constrained to the finest grid size by the CFL (Courant-Friedrich-Lévy) condition. Thus, refinement of the grid size at the vent significantly increases the total execution time due to the increased total number of cells and decreased time-step.

Boundary conditions also play an essential role in the flow dynamics of volcanic plumes. In general, they have been imposed in such a way that their effect is not a primary one (i.e., boundaries are far enough from the plume and large-scale effects are not appreciable). In SK-3D, a free-slip condition is applied at the ground surface boundary, whereas the inflow/outflow conditions were implemented at the upper and other boundaries of the computational domain. In ATHAM, a no-slip boundary condition is imposed at the ground surface, whereas the upper boundary is set to a constant pressure. The lateral boundary conditions are determined from the atmospheric background profile for flow, temperature, and water vapour in the case of inflow, whereas for outflow conditions, the predicted model quantities are advected

towards the boundaries (Oberhuber et al., 1998). In ASHEE, a no-slip boundary conditions is imposed at the ground surface, whereas the atmospheric boundary conditions are designed to allow the outflow of eddies by adopting the Bernoulli approximation on the pressure and inflow/outflow conditions for the other variables. In PDAC, a no-slip boundary condition is applied at the ground surface; at the lateral boundaries, zero-gradient conditions are imposed for outflow, whereas only atmospheric air is allowed at inflow; constant pressure is imposed at the top boundary.

2.3 Input parameters

Two sets of input parameters for a *weak* and a *strong* plume were provided, as described in Costa et al. (2016). The volcanological input parameters, meteorological profiles and physical properties are reported in Table 3 (see Fig. 1 in Costa et al., 2016 for the detail profiles).

In the weak plume case, we set the eruption and meteorological conditions similar to those of the 26 January 2011 Shinmoe-dake eruption (e.g., Kozono et al., 2013; Suzuki and Koyaguchi, 2013). The mass eruption rate was set to 1.5×10^6 kg s^{-1}. The vertical profiles of atmospheric temperature, density, and pressure were based on the meteorological reanalysis data provided by Japan Meteorological Agency's Non-Hydrostatic Model (Hashimoto et al., 2012) for Shinmoe-dake volcano at 00 JST of 27 January 2011 (the profiles are shown in Fig. 1A in Costa et al., 2016). In this case, the atmosphere was cold and dry; the temperature and specific humidity at the ground (1500 m above sea level) were -4.4 ^{o}C and 0.68 g kg^{-1}, respectively. The mean lapse rate is -4.5 K km^{-1} below 17 km and 2.3 K km^{-1} above it.

In the strong plume case, the eruption and meteorological conditions were similar to those of the 15 June 1991 Pinatubo eruption (e.g., Holasek et al., 1996). The

mass eruption rate was $1,000\times$ that of the weak plume: 1.5×10^9 kg s^{-1} (e.g., Suzuki and Koyaguchi, 2009). The atmospheric conditions were based on the reanalysis data obtained from European Centre for Medium-Range Weather Forecasts (ECMWF) by Costa et al. (2013) for Pinatubo volcano at 13:40 PLT of 15 June 1991 (the profiles are shown in Fig. 1B in Costa et al., 2016). The vertical profiles of atmospheric properties were obtained by modifying the ECMWF data as described in Costa et al. (2013). These conditions are more typical of a tropical atmosphere. The temperature and specific humidity at the ground (1500 m above sea level) are 17 ^{o}C and 13.5 g kg^{-1}, respectively. The mean lapse rate is -6.4 K km^{-1} below 17 km and 2.7 K km^{-1} above it.

3. Temporal and spatial filtering of 3D model results

Three-dimensional simulations of eruptive plumes show significant fluctuations in time and space. Therefore, time averaging and spatial integration of the 3D flow fields are necessary to compare results among the 3D models and 1D integral models. In this section, we define and discuss these filtering methods.

3.1 Temporal averaging

To compare the global features obtained by the different 3D models, we first computed the time-averaged distributions of the main dynamic and thermodynamic variables at each grid point in the 3D computational domain. The main variables need to be averaged over an appropriate time window [t_1:t_2]. This should be selected so that by t_1 the plume has already reached a statistically stationary configuration – i.e., it has reached its maximum height and the lateral flow in the umbrella has established. Furthermore, [t_1:t_2] should be longer than the typical timescale of height oscillations. Whereas ASHEE performed a time-averaging runtime (i.e., the average was computed

every time-step), ATHAM and PDAC saved the model output every 1 sec. In SK-3D, the output interval is 1 sec for the weak plume case and 10 sec for the strong plume case. The distributions of the time-averaged fields on vertical cross-sections passing through the vent axis were compared using the same scale and colour contours, using the open-source visualization package Paraview.

3.2 Spatial averaging for vertical profiles

To quantitatively compare the results from different models, *integral variables* of the main flow parameters were obtained as a function of the vertical coordinate (Z). These were cross-sectionally averaged across the plume axis. By post-processing 3D results, each research group produced an ASCII text file containing the following variables as a function of height above sea level, Z:

- Z (height in m);

- R (plume radius in m);

- X-position of plume axis (in m);

- Y-position of plume axis (in m);

- ρ (plume density in kg m^{-3});

- T (plume temperature in ^{o}C);

- V (plume velocity in m s^{-1});

- m_a (entrained air mass fraction);

- m_g (gas mass fraction);

- m_p (pyroclasts mass fraction);

The spatial integration requires the definition of the plume boundaries. For obtaining integral values at each height, we use the method proposed by Cerminara

(2015). This method and four other averaging methods that we have tested are summarized in the Appendix B.

3.3 Definitions of the characteristic plume heights

We defined three characteristic heights of the eruptive plumes: maximum height, height of the neutral buoyancy level (NBL), defined where the mean density of the plume equals that of the atmosphere, and level of maximum radial spreading, defined as the height with the maximum injection of particles. As mentioned previously, these heights show an oscillatory behaviour through time, which requires averaging over a time window to provide consistent results for comparison among models.

The maximum heights were estimated from the highest level in the atmosphere containing volcanic particles (above a critical concentration threshold) at each time step, then averaged across the specified time window. The choice of the critical threshold of particles used to define the edge of the plume, and the time window for averaging, were both decided *a posteriori* based on the sensitivity of results.

Neutral buoyancy level was estimated on the basis of the time-averaged, vertical profile of plume density, defined as the level where the density difference relative to the atmospheric changes sign from negative to positive.

Level of maximum radial spreading was estimated using horizontally-integrated profiles of the particle mass fraction. We radially-integrated the particle mass in the atmosphere, obtaining a vertical profile which was averaged over the time window. Spreading level was then estimated as the height containing the greatest mass of airborne particles.

4. General features of the simulated plumes

To provide a general overview of the behaviour of the weak and strong plumes, this section describes the basic features of the simulations using the SK-3D model as an example. Similarities and differences among the different models are discussed in detail in Section 5.

4.1 Integral variables

Both the weak and strong plumes develop through four main different stages or regions, identified from the integral variables and on vertical slices of the main flow variables (Figs. 1 and 2). In a practical sense, the *jet* region is defined as the momentum-driven flow in the lower column, characterized by a high concentration of particles and density greater than ambient, whereas the *buoyant plume* region is the buoyancy-driven flow with below-ambient density. The *overshooting top* has density greater than atmospheric and collapses downward and outward to feed the *umbrella* region, which spreads radially as a gravity current (e.g., Costa et al., 2013). It is worth noting that a more rigorous definition should be based on the relative momentum and buoyancy fluxes (Morton et al., 1956).

For the weak plume, the eruption column simulated by the SK-3D model (similarly to the other models) reaches its maximum height at about $t = 300$ s. In Fig. 1, we show the instantaneous flow field at $t = 600$ s, when the stationary regime has established and the plume has already spread to a distance of about 5 km from vent (Fig. 1a). In the jet region, below about 2.5–3 km above sea level (asl), the eruption column has an inner core with a mass fraction of the erupted material greater than 0.9 (Fig. 1b) and density larger than the ambient air (Fig. 1c). At the radial boundary between the eruptive jet and ambient air, an outer shear layer develops surrounding

14

the inner core region (e.g., Suzuki et al., 2016). The outer shear layer erodes the inner core, which disappears at about 3 km asl. At this point, the density of the cloud becomes lower than the ambient, and rises as a buoyant plume.

In the plume region, the axis of the volcanic plume oscillates horizontally and exhibits a meandering instability (Suzuki et al., 2005), which could cause efficient mixing with ambient air (see the region from 3–8 km in Fig. 1b). The mass fraction of erupted material (solid particles plus volcanic gases) decreases with height (Fig. 1b) and the plume density and temperature approach those of the atmosphere (Figs. 1c and 1d) due to air entrainment. Around a height of 9 km asl, the plume density and temperature reach nearly ambient values, and the erupted mixture begins to spread out radially. However, the plume top continues to overshoot, oscillating around the level of neutral buoyancy, and reaching a maximum height of 13 km asl. In the overshooting region, from 9 and 13 km asl, the plume is more dense than the atmosphere but has a colder temperature, referred to as "cloud top overcooling" (Woods and Self, 1992). The occurrence of the cloud top overcooling is explained by the adiabatic decompression of the clouds in the stratified atmosphere (e.g. Suzuki and Koyaguchi, 2009).

In the strong plume, the SK-3D model produces a large-scale eruption column that affects the whole stratosphere. The plume reaches its maximum height at about $t = 400$ s. In Fig. 2, we show the instantaneous flow field at $t = 900$ s, when the stationary regime has established and the umbrella has already spread to a distance of about 80 km (Fig. 2a). The eruption column in the jet regime (below about 7 km asl), has a characteristic fountain shape, with a horizontally spreading, yet suspended flow clearly visible at the top of the jet (Neri and Dobran, 1994; Suzuki and Koyaguchi, 2012). This fountain has developed because the outer shear layer was unable to reach

15

the central axis before depletion of the initial momentum (e.g., Suzuki et al., 2016). As a result, the inner, dense core is maintained up to about 7 km asl, where it spreads outward (Fig. 2c). At the margins of the fountaining structure there are large vortices, which vigorously entrain the ambient air, marking the transition to the plume stage. As described in Section 5, it is worth noting that partial column collapse and pyroclastic flows generation occurs in some models, whereas these phenomena are insignificant in SK-3D.

In the buoyant plume region, the mass fraction of the erupted material is much greater than in the corresponding region of the weak plume (by about an order of magnitude), and comparable to the gas mass fraction (Fig. 2b). In contrast to the weak plume, the strong plume maintains high temperatures in the buoyant plume region (Fig. 2d), and accelerates significantly (Fig. 2e), achieving vertical velocities comparable to those at the vent (superbuoyant regime; Bursik and Woods, 1991). Above the neutral buoyancy level, the density increase is much sharper than in the weak case (Figs. 1c and 2c) and the plume manifests a large overshooting top with density greater than atmospheric.

The cloud reaches about 40 km asl and spreads radially from about 20–30 km asl as an umbrella cloud. The umbrella cloud thins with distance from the vent, and the mass fraction of the erupted material decreases at the margins. The over-cooling of the top of the cloud is also observed (Figs. 2d).

4.2 Maximum plume height

Figure 3a shows the time evolution of the maximum height, using different mass fractions thresholds to define the edge of the plume. The thresholds used range from 0.05 to 10^{-5} of the concentration at the vent. In the weak plume case, maximum

height increases until $t = 100$ s from the start of the eruption. After 100 s, the height

defined by the 0.05 threshold fluctuates around 8 km asl (SK-3D results, panel A). In

contrast, maximum heights defined by mass fractions of 0.01 and 0.001, down to 10^{-5}

(PDAC results) are almost identical, rising until 300 s and levelling out at about 12

km asl. On the basis of these results, we use the mass fraction of 0.01 to define the

edge of the plume.

In addition, we tested two different time windows for averaging: [300s:600s]

and [600s:660s]. The first time window is sufficiently longer than the period of

oscillation of the curve corresponding to a fraction of 0.01. However, we also verified

that the time-averaged maximum height does not vary greatly between these two time

windows; the difference is within 10% of the maximum height.

The time evolution of maximum height for the strong plume case is shown in

Fig. 3a. Results of SK-3D using thresholds of 0.05, 0.01, and 0.001 show almost the

same behaviour. Therefore, it is reasonable to define the edge of the plume using a

mass fraction threshold between 0.05 and 0.001. For PDAC, significant dependence

of the plume height on the concentration threshold was observed in the transient stage

of cloud overshooting, due to decoupling of the gas and particulate phases. This

spreading is reduced after 900 s, when the time-average is performed.

The heights increase through time until $t = 400$ s and stabilize around 40 km asl.

For the strong plume case, we tested two time windows for averaging: [600s:1400s]

and [900s:960s]. As for the weak plume case, the difference between averaging

windows is about 10% of the maximum height.

In the inter-comparison, we tentatively use the mass fraction thresholds of 0.01.

17

4.3 Level of maximum radial spreading

The level of maximum radial spreading was estimated from the peak injection of particles. Figure 4 shows the vertical profiles of particle mass fraction, integrated horizontally in the regions where radial spreading dominates the flow ($r > 3$ km for the weak plume case and $r > 30$ km for the strong plume case, where r is the radial distance from the central axis of the plume).

In the weak plume, the umbrella cloud is thin (< 5 km) and has a peak value at 9.4 km asl. In the strong plume, the umbrella cloud is thicker than 10 km and has a peak particle mass fraction at 29.8 km asl. These heights are not strongly dependent on the region of horizontal integration. For example, spreading level changes $< 5\%$ when different regions are selected for the horizontal integration ($r > 5$ km for the weak plume case and $r > 50$ km for the strong plume case).

5. Results of the 3D model inter-comparison

The large-scale features of weak and strong plumes simulated with the different models are qualitatively similar to those described in the previous section, which used results from the SK-3D model as an example. In this section, we quantitatively compare the time-averaged results of the different models, focusing on the plume heights and integral variables. Due to the limitation of computational resources and the overall consistency among the models, we selected a time window for averaging of [600s:660s] for the weak plume, and [900s:960s] for the strong plume, as described in Section 4.2. We have tested the influence of the time-window on the averaged results (results are presented in Fig. 5 for the SK-3D and the PDAC codes). The vertical profiles are extremely stable in the Weak Plume case, while they show a significant variation in the Strong Plume case, although the qualitative

behaviour and the maximum plume height are roughly consistent. Esposti Ongaro and Cerminara (2016) have also shown that the chosen time-window might be too short to smooth fluctuations out and to reproduce the self-similar features of the horizontal profiles. Unfortunately, this problem was not foreseen when the simulations were set up and it was not possible to make longer averages for all models, because the time-averages of ATHAM and ASHEE simulations have been made during runtime. Further detailed investigations of effects of time averaging should be done in future work.

5.1 Vertical cross-sections

Figure 6 shows the time-averaged, vertical cross-sections of particle mass concentration obtained from the different 3D models for the weak plume case, assuming a perfectly windless atmosphere. The large-scale features are similar among all models, displaying a jet from the vent and radial spreading of the buoyant plume region. The flow near the vent entrains ambient air by the shear at the edges of the plume, forming an annular mixing layer surrounding the high concentration core. The formation of the shear layer is hindered in PDAC, probably because of the lower spatial resolution at the vent. Around heights of 8–10 km asl, the cloud spreads radially developing the umbrella region. One notable difference is that ATHAM shows a small proportion of the overshooting plume top reaching about 19 km asl, whereas the other models only reach 13–14 km asl. However, in terms of mass this is a not significant difference as the vast majority of particles ($> 99\%$) are below 14 km asl for all simulations. The atmospheric conditions for the weak plume are cold and dry so that the ambient moisture cannot explain this difference. Furthermore, it is likely that the weak overshoot would be sheared off in a more realistic atmospheric profile with a crosswind. In fact, in ATHAM subgrid turbulence needs some time to

develop. This leads to an underestimate of entrainment at the beginning of the simulation and to a strong overshoot that goes away as the simulation continues. Such a transient behaviour is corrected as soon as a small wind is added in the background (even a wind with 0.5 m/s intensity is enough).

For the strong plume in a windless atmosphere, the time-averaged, vertical cross-sections also show similar features among models (Fig. 7). In contrast to the weak plume, a high-concentration column rises to 5–10 km asl (red color in Fig. 7). Above this height, the cloud entrains substantial amounts of ambient air, leading to a rapid decrease in the particle concentration. For all models the plumes reach 33–43 km asl, forming large spreading umbrella clouds. In the simulation of SK-3D, all the inlet becomes buoyant without collapsing flow. For the other three models, we have computed the percentage of collapse as the maximum value across horizontal slices of the downward mass flow rate of solid particles, estimated on the time-averaged plume field (this is analogous the procedure adopted by Esposti Ongaro et al., 2008). Collapse in the simulation of PDAC constitutes about 7.5 % of the mass flow rate at the inlet, whereas in ASHEE it is slightly larger (about 17 %). In PDAC and ASHEE, almost 100 % of the collapsing mass is re-entrained in the jet or enters buoyant convection as a co-ignimbrite plume merging with the main central plume. In the simulation of ATHAM, almost all the erupted material collapses and subsequent co-ignimbrite plume develops.

There are some important differences among models for this case. In particular the plume undergoes partial collapse and generates pyroclastic flows in ATHAM and, to a lesser extent, in ASHEE, whereas pyroclastic flows are minor (or absent) in PDAC and SK-3D. A common feature among the models is that the jet develops a fountain structure at about 5–10 km asl, with a radially suspended flow at the jet top.

In ATHAM and ASHEE, this fountain periodically collapses, creating pulses of pyroclastic flows (Di Muro et al., 2004; Ogden et al., 2008; Van Eaton et al., 2012). In contrast, the fountain is more stable in PDAC and SK-3D, with the majority of the plume continuing to rise buoyantly. Although we still cannot provide a detailed explanation of the different collapsing behaviour, we notice that the Strong Plume inlet conditions are close to the threshold between the buoyant and collapsing regimes. Unstable regimes are more sensitive to small perturbations, enhancing differences among simulations.

Another interesting difference is that the buoyant region (10–40 km asl), contains lower particle concentrations in ATHAM and SK-3D compared to ASHEE and PDAC. Moreover the plume height predicted by PDAC is 10 km larger than those of the other models. However, it is worth noting again that, as shown in Fig. 4, such differences might be affected by the time-window used for averaging.

5.2 Plume heights

The characteristic plume heights (maximum height, NBL, and spreading level) were estimated by applying the time averaging described in Section 3.1 and spatial filter *f4* (see Appendix B). Results are reported in Tables 4 and 5, and illustrated in Fig. 8.

For the weak plume, all models produce consistent NBL and spreading level with standard deviations of about 9 and 13%, respectively. The standard deviation of the maximum height (22%) is greater than for NBL and spreading level. As explained above, the maximum height predicted by ATHAM is higher than those in the other models, with a dilute, overshooting top rising to 19 km asl (Fig. 6). These differences

21

may be related to numerical diffusion of the discretization schemes and turbulence parameterizations used in the different models.

For the strong plume, the NBL and spreading level depend more significantly on which model is used; the standard deviations reach 24%. The maximum estimates of NBL and spreading level (by PDAC) are 12–13 km larger than the minimum estimates (by ATHAM). The estimated maximum height has relatively small standard deviation of 10%, but the difference between the maximum and minimum values is 11 km. ATHAM predicts lower NBL, spreading level, and maximum height than those given by the other models. This difference may be explained by episodic collapse of the column, which reduces the overall amount of buoyant mass.

5.3 Profiles of integral variables

We obtained profiles of horizontally-integrated variables by applying filter *f4* (see Appendix B) to the 3D results. Figs. 9 and 10 shows profiles of entrained air fraction, density, gas fraction, plume radius, mass fraction particles, temperature, and velocity, for the weak and strong plume cases.

For the weak plume, vertical profiles are similar among the different 3D models (Fig. 9), especially in the buoyant plume region. Furthermore, as discussed in the companion paper by Costa et al. (2016), they do not differ greatly from those predicted by integral 1D models. In the lower part of the eruptive column, the mass fractions of gas, particles, and entrained air show some interesting differences. The entrained air fraction predicted by ATHAM and SK-3D increases more rapidly than in ASHEE and PDAC (Fig. 9a). As a result, the decrease in density and temperature in ATHAM and SK-3D is more rapid (Fig. 9b and 9f). The variation in radius below the umbrella region (< 8 km; see Fig. 6) is several hundred meters (Fig. 9d).

Superbuoyancy develops strongly in SK-3D (indicated by the sharp increase in velocity above the jet region), whereas it is not so evident in the other models (Fig. 9g).

For the strong plume, the models appear to vary significantly in terms of the integral variables (Fig. 10). Differences are particularly relevant in the profiles of mixture components (particles, gas, entrained air). The increase of entrained air fraction, and the decrease of density, particle fraction, temperature, and velocity in ATHAM show sharper gradients than those in the other models, likely due to the stronger collapse regime and generation of pyroclastic flows. Even though SK-3D, ASHEE, and PDAC generate a relatively more stable column, the decrease in entrained air fraction still shows significant differences. The entrained air fraction decreases more rapidly in SK-3D than in ASHEE and PDAC, but the resultant entrained air fraction in the buoyant region is larger than those in ASHEE and PDAC (Fig. 10a). The column radii are similar in each model in the jet and buoyant region (< 15 km in Fig. 10d), yet vary significantly in the umbrella region. It is worth noting that the condition of considering vertical velocity $w > 0$ excludes the umbrella region from the calculation of the average plume profile, also in the case of the limited lateral domain of the ASHEE and PDAC simulations.

5.4 Entrainment coefficient

Local entrainment coefficients for the weak and the strong plume cases can be computed from the profiles of integral variables as $\alpha = dQ/dz \, Q/(2\rho_a b M)^{-1}$ (M is the momentum flux, Q is the mass flux, ρ_a is the atmospheric density, and b is the plume radius). We remark here that, because Q in 3D simulations is influenced by particle fallout and re-entrainment, the obtained entrainment coefficient implicitly accounts

23

for these phenomena. Since all the quantities are a function of the height, the resulting entrainment coefficient is variable along the plume. Its value for the four different models is reported in Fig. 11.

The weak plume simulations predict a value of the entrainment coefficient around 0.1 in the buoyant plume region (i.e., where the flow is in the Boussinesq regime), which is relatively consistent with laboratory observations (Morton et al., 1956). On the contrary, simulations of the strong plume show greater variability, and the entrainment in the buoyant plume region is much higher than 0.1 ($\alpha > 0.2$). It is also worth remarking that, in the strong plume, partial collapse episodes make the prediction of the entrainment coefficient in the jet region more uncertain (see Discussion below).

The estimated value of the entrainment coefficient varies among the numerical models. This variation could be attributed to the procedure of estimation such as the choice of time-window, and the accuracy of scheme. In particular, because the value of the entrainment coefficient is computed by using the deviation of mass flux (i.e., *dQ/dz*), the value is sensitive to the averaging method. For further investigation, robust methods such as a low pass filtering are required.

Finally, in the umbrella region, the 1D entrainment assumption is no longer satisfied because the horizontal flow is predominant, so the value of the entrainment coefficient is less significant. In this case, alternative entrainment rate should be used (e.g., Samasiri and Woods, 2015) and its value needs to be quantified using 3D simulations.

5.5 Wind effects

The simulations which include the effects of wind were carried out using ATHAM and SK-3D only (Fig. 12). In the simulations of the strong and weak plumes in windy conditions, the same eruption and atmospheric parameters were used as in Table 3.

In the weak plume case, ATHAM and SK-3D show similar features (Figs. 12a and 12b). Even near the vent, the eruption columns are largely distorted by the wind. At 2–3 km asl, there are the kink structures (see arrows in Fig. 12a and 12b). These kinks can be explained by changes in the wind direction with height. The column reaches 7 km asl when the plume extends about 7 km downwind from the vent in ATHAM, whereas this distance is reduced to 3 km downwind in SK-3D. At $x > 10$ km, the clouds move horizontally and are elongated up to $x = 25$ km. The horizontally moving cloud in ATHAM is thicker than that in SK-3D.

In the strong plume case, the results from ATHAM (Fig. 12c) and SK-3D (Fig. 12d) are not significantly affected by wind by comparison with Figs. 7a and 7b, respectively. This is because the eruption intensity is large (exit velocity 275 m s^{-1}) compared to the wind intensity (maximum velocity is 21 m s^{-1} at 16 km asl). Hence, the effect of wind is small. As in the windless case, the percentage of collapse in ATHAM is significant and the plume is mainly formed by re-entrainment of the solid material and formation of a co-ignimbrite. Pyroclastic flows are thus shed from the column in ATHAM, whereas none are produced in SK-3D. This is likely the main reason for ATHAM's lower maximum height and NBL compared to SK-3D, although gravitational decoupling of particles from the flow field may also play a role (not considered in SK-3D, see also Table 6). Due to the lack of pyroclastic flows in SK-3D, the umbrella cloud expands more rapidly than in ATHAM.

25

We also compared the plume heights calculated by the 3D models with those predicted by the 1D models (Table 6). In the weak plume case, the maximum heights are higher than those predicted by the 1D models, and the NBLs are slightly higher (several hundred meters) than the mean values of the 1D estimates. In the strong plume case, the maximum height in ATHAM is almost the same of the 1D estimates, whereas that in SK-3D is substantially higher than the 1D estimates. The NBLs in ATHAM and SK-3D are 6–8 km lower than the 1D estimates.

6. Discussion

As shown in Figs. 9 and 10 and commented in Sections 5.1 and 5.3, models show greater variability in the strong plume than in the weak plume case.

We propose, as a possible explanation for these apparent discrepancies, that variability in the different physical and numerical formulations are enhanced in the strong plume scenario. There, the plume dynamics are driven by sharp density and temperature contrasts (even in the buoyant plume region) and by a distinct jet-plume transition, with large accelerations and momentum/heat exchange occurring on relatively short timescales. Therefore, in the following sections, we briefly examine some of the possible sources of diversity among the results, leaving a more rigorous investigation to future detailed studies.

6.1 Non-equilibrium gas-particle effects

Non-equilibrium effects between gases and particles are treated in different ways in the four models, from complete equilibrium (SK-3D), to full non-equilibrium (PDAC), through inclusion of settling (ATHAM), and preferential concentration and settling (ASHEE).

The relevance of non-equilibrium effects can be estimated on the basis of a

26

simple scaling consideration using the particle Stokes number which represents the ratio of a reference flow characteristic time scale $\tau_f = D/U$ (D and U being the vent diameter and vertical velocity, respectively) and the Stokes time scale of gas-particle interaction τ_p (estimated from the particle density, diameter, and the viscosity of flow). The weak plume was initialized with coarser particle sizes than the strong plume (1mm and 62.5 μm vs. 0.5mm and 15.6 μm). This leads to larger particle Stokes numbers ($St_{coarse} \sim 5$, $St_{fine} \sim 0.25$ for the weak plume vs. $St_{coarse} \sim 0.25$, $St_{fine} \sim 0.001$ for the strong plume), suggesting that non-equilibrium effects are more relevant in the weak plume case. Adopting an alternative definition of the fluid timescale based on the Taylor microscale (Cerminara et al., 2016b) confirms such a preliminary analysis. This scaling consideration suggests that it is less likely that discrepancies in the strong plume simulations are due to the different treatment of non-equilibrium effects among the models. It calls for further consideration and systematic numerical simulations using a non-equilibrium model. More detailed investigations of the influence of multiphase flow effects are taken up in Esposti Ongaro and Cerminara (2016) and Cerminara et al. (2016b).

6.2 Jet dynamics

Strong plume development is particularly sensitive to the dynamics below the region of buoyancy reversal (jet region). This extends over about $1/8^{th}$ of the maximum plume height in the strong plume case, while it is limited to about $1/40^{th}$ in the weak plume case (see Figs. 9b and 10b).

This region manifests different degrees of instability, leading to the observed fountaining structure and episodic partial collapse, with formation of pyroclastic density currents in some cases (ATHAM, ASHEE, and to a minor extent in PDAC).

Changes in the collapse behaviour lead to major changes in the amount of solids transported in the buoyant plume and thus in the overall dynamics (Van Eaton et al., 2012). Jet instability is very sensitive to source conditions, and the different degrees of instability among the four models may be potentially linked to grid resolution (see section below). Moreover, the different physical formulations or thermodynamic descriptions can be particularly relevant in this region.

We point out that the set of eruptive conditions selected for the strong plume case represent a supersonic flow. The speed of sound in the gas-particle mixture is around 140 m s^{-1} (compared to an exit velocity of 275 m s^{-1}), making the plume *overexpanded* at the vent. The supersonic condition can change the flow properties (Ogden et al., 2008, 2011; Carcano et al., 2014). Description of supersonic regimes is known to be a stiff numerical problem (e.g., Carcano et al., 2013), potentially enhancing sensitivity to model formulation.

6.3 Role of mesh resolution and of subgrid turbulence model

The accuracy of the numerical scheme and the treatment of subgrid turbulence can affect the entrainment process and thus the global features of eruption column dynamics. The mixing efficiency in free boundary shear flows depends mainly on the engulfment process, which is caused by large-eddy motion. To reproduce the engulfment process, a sufficiently high spatial resolution is required. In this inter-comparison, the accuracies of schemes employed by each 3D model are different, and therefore, the adequate grid sizes for each models are necessarily different. If the accuracy of the scheme is low or the grid size is large, the numerical results such as plume heights and critical condition for column collapse may be significantly different (e.g., Suzuki et. al., 2005). For example, in the simulations for

strong plume case using SK-3D, the present results show thea purely buoyant regime, whereas the results with a coarser grid sizes, with $\Delta X_{min} = D/12$ (118 m) and $\Delta X_{max} = 200$ m show partial collapse regime. On the other hand, an additional PDAC simulation with a coarser grid of $\Delta X_{min} = \sim D/13$ (100 m) and $\Delta X_{max} = 1000$ m results in a more radially spreading suspended flows and a slightly lower maximum plume height, although the jet collapse is still a minor one (less than 10%).

Difference in the turbulence model can be also a source of uncertainty in some cases. ASHEE, and PDAC use the LES approach to describe subgrid-scale turbulence, whereas SK-3D adopts the approach described by Suzuki et al. (2005), which does not model subgrid turbulence. Current numerical results support the observation that entrainment rate in the turbulent buoyant plume is imposed by the large-scale eddy motions (e.g., Plourde et al., 2008; da Silva et al., 2014, Cerminara et al., 2016a), thus making less relevant the role of the subgrid-scale (LES) turbulence scheme. However, Cerminara et al. (2016b) report that the LES model has a non-negligible effect above the NBL of the strong plume.

7. Concluding Remarks

We have presented results from an inter-comparison study of four different 3D models of volcanic plume. In the study, a set of common volcanological input parameters and atmospheric conditions were given for two case studies, representing a strong and a weak plume. Comparison of the results indicates that all the models give consistent predictions of the large scale behaviour. In particular, maximum plume heights estimates have a standard deviations of about 20%.

A comparison of the results for the weak plume showed that all models can consistently predict the transition from a jet stage to a stable, self-similar buoyant plume. Vertical plume profiles are very similar among the models and the simulated NBL, spreading level and maximum height differ by less than 2 km (except one case where a transient overshooting was observed).

Simulations of the strong plume show more significant variability. Each model shows the particle-laden jet rising to 5-10 km asl before an instability develops in the form of a fountaining structure. A key difference among models is the extent to which this fountain remains buoyant or undergoes episodic, partial collapse. On one end of the spectrum, essentially no collapse or pyroclastic flows occurs (SK-3D), to minor flows (PDAC), and significant (ASHEE) to very significant (ATHAM). This reflects in significant differences of the mean plume profiles. The generation of pyroclastic flows by partial column collapse also has a significant effect on the amount of mass that rises into the upper atmosphere, leading variations of maximum plume height within 33-43 km and to slower rates of umbrella cloud expansion compared to stable buoyant plumes. Such differences would have an important impact on forecasts of ash dispersal. Furthermore, there are important implications for our understanding of volcanic hazards and predicting the eruptive conditions that lead to small vs. large-volume pyroclastic flows.

A possible explanation for such a different behaviour is that the Strong Plume eruptive conditions are closer to the threshold between the buoyant and collapsing regimes. Since unstable regimes are more sensitive to perturbations, differences among model formulation and numerical approach are there enhanced. The models used in this study employ indeed different numerical procedures, spatial resolutions, subgrid turbulence models, and treatments of multiphase and

microphysical processes. The superposition of all these differences impact the diversity of the results, without allowing us to precisely identify the sources of discrepancy. To quantify the net effect of the numerical solvers, standard benchmarks with equivalent physical formulation and common validation procedures will be specifically designed in the future for all models. In addition, future investigations will be aimed at quantifying the magnitude of the turbulent stress in the different regimes, in order to compare the different LES approaches.

Comparison with one-dimensional models have allowed us to derive an empirical parameterization of the entrainment coefficient, which is highly variable among models and it is particularly poorly constrained for strong plumes and windy conditions. Future studies will potentially provide improved estimates by means of extensive and accurate analysis of 3D simulations, aimed not only at evaluating the mean flow profiles but also the statistics of turbulent fluctuations. Furthermore, it is worth highlighting that 1D models do not account for partial collapse or over/underexpanded regimes, which likely accounts for some of the systematic discrepancies between 1D and 3D models (Costa et al., 2016).

Appendix A

To clearly indicate the difference of grid sizes employed by each models, the vertical grid sizes are expressed as a function of height (Fig. A1).

Appendix B

Five different methods were proposed for obtaining integral values at each height from 3D simulation results. In this appendix, we introduce these methods and discuss the advantages and limitations of each one.

f1) The simplest option defines the plume boundary by the concentration of erupted material. The plume radial-scale, L, is defined where the mass fraction of a passive tracer (such as water vapor) reaches a small fraction of its maximum value, (e.g., 0.1%; Suzuki and Koyaguchi, 2009). The integral variables ρ, T, V, m_a, m_g, and m_p are radially averaged within $r < L$, where r is the radial distance from the axis of the plume. If this filter is applied, the flow field inside L can include regions with negative velocity.

f2) The second method assumes that radial profiles of the different physical properties can be described through a Gaussian function:

$$f(r) = f(r_c)\exp\left(-\frac{r^2}{b^2}\right), \tag{A1}$$

where r denotes the radial coordinate perpendicular to the plume axis, r_c represents the centreline, and the radial scale b indicates the distance at which the generic quantity f decays by a factor e. In this choice, the plume radial-scale

is *b*. Note that the top-hat radius is given by $L^2 = R^2 = 2b^2$ (e.g., Davidson, 1986). In this way the variables can be estimated from the peak values, i.e., f (r_c).

Alternative methods are based on the evaluation of the average quantities over a horizontal domain $\Omega(z)$ defined, at each height *z*, by the conditions [$w > 0$; $tr > tr_c$], where *w* is the vertical velocity and $tr > tr_c$ indicates the condition that concentration of the tracer *tr* is larger than the threshold tr_c. Such a choice is consistent with the hypotheses of 1D models, assuming a positive vertical velocity in the plume.

f3)   The third method uses an approach similar to Kaminski et al. (2005) on the basis of momentum and buoyancy fluxes and reduced gravity:

$$\pi R^2 W^2 = \int_\Omega w^2 dxdy, \tag{A2}$$

$$\pi R^2 G' = \int_\Omega g' dxdy, \tag{A3}$$

$$\pi R^2 W G' = \int wg' dxdy, \tag{A4}$$

where *x* and *y* are the horizontal axis, *w* denotes the local value of the vertical plume velocity, g' is the local reduced gravity, *R* is the top-hat radial length scale, *W* is the top-hat velocity scale, and G' is the top-hat reduced gravity scale. In order to obtain the mean values of the mass fraction of the ejected material *S*, and the temperature *T*, a similar approach is applied:

$$\pi R^2 WS = \int_\Omega w\xi dxdy, \tag{A5}$$

$$\pi R^2 WT = \int_\Omega w\theta dxdy, \tag{A6}$$

where ξ and θ are the local values of the mass fraction of the ejected material and the temperature, respectively. This method is effective only in the Boussinesq approximation (when the mixture density very similar to the atmospheric density).

f4) The fourth choice represents a generalization of the method *f3* and the definition of the mean values is consistent with the formulae of the steady 1D models (see Cerminara, 2015 and Cerminara et al., 2016b for more detail on the derivation). This method is based on the mass, momentum and enthalpy (instead of buoyancy) fluxes, to take into account large density contrasts between the plume and the surrounding atmosphere (non-Boussinesq regime);

$$F_1^{(iv)} = \int_\Omega \rho w \, dx \, dy, \tag{A7}$$

$$F_2^{(iv)} = \int_\Omega \rho w^2 \, dx \, dy, \tag{A8}$$

$$F_3^{(iv)} = \int_\Omega \rho x w \, dx \, dy, \tag{A9}$$

$$F_4^{(iv)} = \int_\Omega \left(\frac{1+\sum_i(\gamma_i-1)x_i}{1+\sum_i(\varphi_i-1)x_i} \rho_a - \rho \right) w \, dx \, dy, \tag{A10}$$

where γ_i is the ratio between the specific heat at constant pressure of the *i*th phase class and that of the atmosphere, φ_i is the ratio between the gas constant of the *i*th phase class and that of the atmosphere.

The plume radius, and the mean values of plume density, mass fractions of *i*th class, plume temperature, velocity are estimated by using inversion formulae;

$$L = \sqrt{\frac{F_1^{(iv)}(F_4^{(iv)}+F_1^{(iv)})(F_1^{(iv)}+Q_\varphi)}{\pi \rho_a F_2^{(iv)}(F_1^{(iv)}+Q_\gamma)}}, \tag{A11}$$

$$\bar{\rho} = \rho_a \frac{F_1^{(iv)}(F_1^{(iv)} + Q_\gamma)}{(F_4^{(iv)} + F_1^{(iv)})(F_1^{(iv)} + Q_\varphi)}, \tag{A12}$$

$$S_i = \frac{Q_i}{Q}, \tag{A13}$$

$$\bar{T} = T_a \frac{F_4^{(iv)} + F_1^{(iv)}}{F_1^{(iv)} + Q_\gamma}, \tag{A14}$$

$$W = \frac{F_2^{(iv)}}{F_1^{(iv)}}, \tag{A15}$$

where T_a is the atmospheric temperature and ρ_a is the atmospheric density.

f5) The fifth filter is analogous to *f3* and *f4* but it is built upon the internal energy flux (instead of enthalpy), and the mixture density is evaluated on the basis of the average pressure:

$$F_1^{(v)} \equiv \pi \bar{\rho} R^2 W = \int_\Omega \rho w \, dx dy, \tag{A16}$$

$$F_2^{(v)} \equiv \pi \bar{\rho} R^2 W^2 = \int_\Omega \rho w^2 \, dx dy, \tag{A17}$$

$$F_3^{(v)} \equiv \pi \bar{\rho} X R^2 W = \int_\Omega \rho \xi w \, dx dy, \tag{A18}$$

$$F_4^{(v)} \equiv \pi \bar{\rho} E R^2 W = \int_\Omega \rho e w \, dx dy, \tag{A19}$$

where ρ denotes the local value of density, e is the internal energy, $\bar{\rho}$ is the mean value of density, and E is the mean value of internal energy. The mean values of the velocity, the mass fraction, and the internal energy are easily obtained as

$$W = F_2^{(v)}/F_1^{(v)}, \tag{A20}$$

$$S = F_3^{(v)}/F_1^{(v)}, \tag{A21}$$

$$E = F_4^{(v)}/F_1^{(v)}. \qquad (A22)$$

The mean values of the heat capacity $\bar{C}_v$ and gas constant $\bar{R}_{gas}$ are obtained using S. The mean value of the pressure $\bar{P}$ is estimated from a horizontal average as:

$$\bar{P} = \int_\Omega P \, dxdy \, / \int_\Omega \, dxdy, \qquad (A23)$$

where P is the local value of pressure. The mean temperature is calculated by

$$\bar{T} = F_4^{(v)}/\left(\bar{C}_v \cdot F_1^{(v)}\right). \qquad (A24)$$

Then, the mean density is estimated using the equation of state;

$$\bar{\rho} = \bar{P}/\left(\bar{R}_{gas}\bar{T}\right). \qquad (A25)$$

Finally, the radial length scale R is given as

$$R = \frac{F_1^{(v)}}{(\bar{\rho} \cdot F_2)^{1/2}} \, . \qquad (A26)$$

In the following, we compare the results of radial integrations using the different averaging filters proposed above. First of all, because of the nonlinear change of volcanic plume density, the radial profiles of physical quantities such as density cannot be described by the Gaussian profiles (see Fig. 4a in Suzuki and Koyaguchi, 2010). Therefore, $f2$ is not appropriate to obtain the vertical profiles from the 3D simulation results.

Figure B1 shows the vertical profiles of the variables using *f1*, *f3*, *f4*, and *f5* for the simulations of SK-3D. The variables obtained by using *f3* fluctuate much more strongly with height than those obtained by the other filters. There are rapid increases in entrained air fraction and rapid decreases in upward velocity at 1.8 km. There are also rapid decreases in entrained air fraction, and rapid decreases in upward velocity at 8.2 km. These abrupt changes of the quantities are caused by the fact that the derived variables can become zero or infinity when the sign of *G'* switch. The filter *f3* is thus not appropriate to obtain the vertical profiles in volcanic plume.

The vertical profiles obtained by *f1*, *f4*, and *f5* show similar features. In particular, *f4* and *f5* provide almost same profiles of the variables. In the jet region near the vent, the entrained air fraction based on *f1* increases more rapidly than those based on *f4* and *f5*. In such a region, the annular downflow region develops around the main stream of eruption clouds, so that the average values computed by *f1* are unrealistic. For the model inter-comparison, we chose the filter *f4* which is based on the exact derivation of a generalized 1D model (Cerminara, 2015).

References

Balachandar, S., Eaton, J. K., 2010. Turbulent dispersed multiphase flow. *Annu. Rev. Fluid Mech*. 42, 111–133.

Bursik, M., 2001, Effect of wind on the rise height of volcanic plumes. Geophys. Res. Lett. 28(18), 3612–3624. doi:10.1029/2001GL013393.

Bursik, M., Woods, A. W., 1991. Buoyant, superbuoyant and collapsing eruption columns. *J. Volcanol. Geotherm. Res*. 45, 347–350.

Carcano, S., Bonaventura, L., Esposti Ongaro, T., Neri, A., 2013. A semi-implicit, second-order-accurate numerical model for multiphase underexpanded volcanic jets. *Geosci. Mode Dev*. 6, 1905–1924. http://dx.doi.org/10.5194/gmd-6-1905-2013.

Carcano, S., Esposti Ongaro, T., Bonaventura, L., Neri, A., 2014. Influence of grain-size distribution on the dynamics of underexpanded volcanic jets. *J. Volcanol. Geotherm. Res.*, 285, 60–80.

Cerminara, M., 2015. The multiphase buoyant plume solution of the dusty gas model. ArXiv: 1506.01638.

Cerminara, M., Esposti Ongaro, T., Berselli, L. C., 2016a. ASHEE 1.0: a compressible, equilibrium-Eulerian model for volcanic ash plumes. *Geosci. Model Dev.,* 9, 697-730, doi:10.5194/gmd-9-697-2016.

Cerminara, M., Esposti Ongaro, T., Neri A., 2016b. Large eddy simulation of gas-particle kinematic decoupling and turbulent entrainment in volcanic plumes. *J. Volcanol. Geotherm. Res.*, submitted (this issue).

Cerminara, M., 2016. Modeling dispersed gas-particles turbulence in volcanic ash plumes. PhD thesis; Scuola Normale Superiore; *to appear*.

Costa, A., Folch, A., Macedonio, G., 2013. Density-driven transport in the umbrella region of volcanic clouds: Implications for tephra dispersion models. *Geophys. Res. Lett.*, 40, 4823–4827. doi:10.1002/grl.50492.

Costa, A., Suzuki, Y. J., Cerminara, M., Devenish, B., Esposti Ongaro, T., Herzog, M., Van Eaton, A. R., Denby, L. C., Bursik, M., de'Michieli Vitturi, M., Engwell, S., Neri, A., Barsotti, S., Folch, A., Macedonio, G., Girault, F., Carazzo, G., Tait, S., Kaminski, E., Mastin, L. G., Woodhouse, M. J., Phillips, J. C., Hogg, A. J., Degruyter, W., and Bonadonna, C., 2016. Results of the eruption column model inter-comparison exercise. *J. Volcanol. Geotherm. Res.*, http://dx.doi.org/10.1016/j.jvolgeores.2016.01.017.

Crank, J., Nicolson, P., 1947. A practical method for numerical evaluation of solutions of partial differential equations of the heat conduction type. *Proc. Camb. Phil. Soc*. 43 (1): 50–67. doi:10.1007/BF02127704.

da Silva, C. B., Hunt, J. C., Eames, I., Westerweel, J., 2014. Interfacial layers between regions of different turbulence intensity. Annu. Rev. Fluid Mech. 46, 567–590. doi:10.1146/annurev-fluid-010313-141357.

Davidson, G.A. 1986. Gaussian versus top-hat profile assumptions in integral plume models. *Atm. Env.* 20 (3), 471–478.

Di Muro, A., Neri, A., Rosi, M., 2004. Contemporaneous convective and collapsing eruptive dynamics: The transitional regime of explosive eruptions. *Geophy. Res. Lett.*, 31(10), L10607–4.

Dobran, F., Neri, A., Macedonio, G., 1993. Numerical simulation of collapsing volcanic columns. *J. Geophys. Res. 98*(B3), 4231–4259.

Elghobashi, S., 1991. Particle-laden turbulent flows: direct simulation and closure modes. *Applied Sci. Res.* 48, 301–314.

Elghobashi, S., 1994. On predicting particle-laden turbulent flows. *Applied Sci. Res*. 52, 308–329.

Esposti Ongaro, T., Cavazzoni, C., Erbacci, G., Neri, A., Salvetti, M. V., 2007. A parallel multiphase flow code for the 3D simulation of explosive volcanic eruptions. *Parallel Computing* 33(7), 541–560.

Esposti Ongaro, T., Cerminara, M., 2016. Non-equilibrium processes in ash-laden volcanic plumes: new insights from 3D multiphase flow simulations, *J. Volcanol. Geotherm. Res.* doi:10.1016/j.jvolgeores.2016.04.004.

Esposti Ongaro, T., Neri, A., Menconi, G., de' Michieli Vitturi, M., Marianelli, P., Cavazzoni, C., Erbacci, G., Baxter, P. J., 2008. Transient 3D numerical simulations of column collapse and pyroclastic density current scenario at Vesuvius. *J. Volcanol. Geotherm. Res*., 178, 378–396.

Fanneløp, T. K., Webber, D. M., 2003. On buoyant plumes rising from area sources in a calm environment. *J. Fluid Mech.*, 497, 319–334.

Ferry, J., Balachandar, S., 2001. A fast Eulerian method for disperse two-phase flow. *Int. J. Multiph. Flow* 27, 1199–1226.

Folch, A., 2012. A review of tephra transport and dispersal models: Evolution, current status, and future perspectives. *J. Volcanol. Geotherm. Res*. 235–236, 96–115. doi:10.1016/j.jvolgeores.2012.05.020.

Hashimoto, A., Shimbori, T., Fukui, K., 2012. Tephra fall simulation for the eruptions at Mt. Shinmoe-dake during 26–27 January 2011 with JMANHM. *SOLA* 8, 37–40.

Herzog, M., Graf, H.-F., 2010. Applying the three-dimensional model ATHAM to volcanic plumes: Dynamics of large co-ignimbrite eruptions and associated

injection heights for volcanic gases. *Geophys. Res. Lett.* 37, L19807. doi:10.1029/2010GL044986.

Holasek, R., Self, S., Woods, A. W., 1996. Satellite observations and interpretation of the 1991 Mount Pinatubo eruption plumes, *J. Geophys. Res.*, 101(B12), 27,635–27,655

Issa, R. I., 1986. Solution of the implicitly discretised fluid flow equations by operator-splitting. *J. Comput. Phys*. 62, 40–65.

Kaminski, E., Tait, S., Carazzo, G., 2005. Turbulent entrainment in jets with arbitrary buoyancy. *J. Fluid Mech*. 526, 361–376.

Kozono, T., Ueda, H., Ozawa, T., Koyaguchi, T., Fujita, E., Tomiya, A., Suzuki, Y. J., 2013. Magma discharge variations during the 2011 eruptions of Shinmoe-dake volcano, Japan, revealed by geodetic and satellite observations. *Bull. Volcanol.* 75, 695. doi: 10.1007/s00445-013-0695-4.

Marble, F. E., 1970. Dynamics of dusty gases. *Annual Rev. Fluid Mech*. 2(1), 397–446.

Mastin, L. G., Guffanti, M., Servranckx, R., Webley, P., Barsotti, S., Dean, K., Durant, A., Ewert, J. W., Neri, A., Rose, W. I., Schneider, D., Siebert, L., Stunder, B., Swanson, G., Tupper, A., Volentik, A., Waythomas, C. F., 2009. A multidisciplinary effort to assign realistic source parameters to models of volcanic ash-cloud transport and dispersion during eruptions. *J. Volcanol. Geotherm. Res*. 186, 10–21. doi:10.1016/j.jvolgeores.2009.01.008.

Moin, P., Squires, K. D., Cabot, W. H., Lee, S., 1991. A dynamics subgrid-scale model for compressible turbulence and scalar transport. *Phys. Fluids A*, 3(11), 2748. doi:10.1063/1.858164.

Morton, B. R., 1959. Forced plumes. *J. Fluid Mech. 5*(01), 151–163.

Morton, B. R., Taylor, G. I., Turner, J. S., 1956. Turbulent gravitational convection from maintained and instantaneous source. *Phil. Trans. Roy. Soc. Lond.*, Ser. A, 234, 1–23.

Neri, A., Dobran, F., 1994. Influence of eruption parameters on the thermofluid dynamics of collapsing volcanic columns. *J. Geophys. Res*. 99 (B6), 11,833–11,857.

Neri, A., Esposti Ongaro, T., Macedonio, G., Gidaspow, D., 2003. Multiparticle simulation of collapsing volcanic columns and pyroclastc flow. *J. Geophys. Res*. 108(B4), 2202. doi:10.1029/2001JB000508.

Oberhuber, J. M., Herzog, M., Graf, H.-F., Schwanke, K., 1998. Volcanic plume simulation on large scales. *J. Volcanol. Geoth. Res. 87*(1), 29–53.

Ogden, D. E., Glatzmaier, G. A., Wohletz, K. H., 2008. Effects of vent overpressure on buoyant eruption columns: Implications for plume stability. *Earth Planet. Sci. Lett.*, 268(3-4), 283–292.

Ogden, D., 2011. Fluid dynamics in explosive volcanic vents and craters. *Earth Planet. Sci. Lett*. 312(3-4), 401–410.

Ogden, D.E., Wohletz, K.H., Glatzmaier, G.A., Brodsky, E.E., 2008. Numerical simulations of volcanic jets: Importance of vent overpressure. *J. Geophys. Res.*, 113, B02204.

Plourde, F., Pham, M. V., Kim, S. D., Balachandar, S., 2008. Direct numerical simulations of a rapidly expanding thermal plume: structure and entrainment interaction. *J. Fluid Mech*. 604, 99–123.

Roe, P. L., 1981. Approximate Riemann solvers, parameter vectors, and difference schemes. *J. Comput. Phys*., 43, 357–372. doi:10.1016/0021-9991(81)90128-5.

Samasiri, P., Woods, A. W., 2015. Mixing in axisymmetric gravity currents. *J. Fluid Mech.* 782, R1. doi:10.1017/jfm.2015.519.

Smagorinsky, J., 1963. General circulation experiments with the primitive equations. *Mon. Weather Rev.* 91, 3–36.

Smolarkiewicz, P. K., 1984. A fully multidimensional positive definite advection transport algorithm with small implicit diffusion. *J. Comput. Phys.* 54, 325–362.

Sparks, R. S. J., Bursik, M. I., Carey, S. N., Gilbert, J. S., Glaze, L. S., Sigurdsson, H., Woods, A. W., 1997. Volcanic Plumes. John Wiley & Sons, Chichester. 574 pp.

Suzuki Y.J., Costa A., Koyaguchi T. (2016) On the relationship between eruption intensity and volcanic plume height: insights from three-dimensional numerical simulations, *J. Volcanol. Geotherm. Res.*, doi:10.1016/j.jvolgeores.2016.04.016.

Suzuki, T., 1983. A theoretical model for the dispersion of tephra. *Arc volcanism: Physics and tectonics*. D. Shimozuru and I. Yokoyama, eds., Terra Scientific Publishing, Tokyo, 95–103.

Suzuki, Y. J., Koyaguchi, T., 2009. A three-dimensional numerical simulation of spreading umbrella clouds. *J. Geophys. Res.* 114, B03209. doi:10.1029/2007JB005369.

Suzuki, Y. J., Koyaguchi, T., 2010. Numerical determination of the efficiency of entrainment in volcanic eruption columns. *Geophys. Res. Lett.*, 37, L05302. doi:10.1029/2009GL042159.

Suzuki, Y. J., Koyaguchi, T., 2012. 3-D numerical simulations of eruption column collapse: Effects of vent size on pressure-balanced jet/plumes. J. Volcanol. Geotherm. Res. 221–222, 1–13. doi:10.1016/j.jvolgeores.2012.01.013.

Suzuki, Y. J., Koyaguchi, T., 2013. 3D numerical simulation of volcanic eruption clouds during the 2011 Shinmoe-dake eruptions. *Earth Planets Space* 65 581–589. doi:10.5047/eps.2013.03.009.

Suzuki, Y. J., Koyaguchi, T., 2015. Effects of wind on entrainment efficiency in turbulent mixing in eruption clouds using a three-dimensional fluid dynamics model. *J. Geophys. Res. Solid Earth* 120. doi:10.1002/2015JB012208.

Suzuki, Y. J., Koyaguchi, T., Ogawa, M, Hachisu, I., 2005. A numerical study of turbulent mixing in eruption clouds using a three-dimensional fluid dynamics model. *J. Geophys. Res*. 110, B08201. doi:10.1029/2004JB003460.

Suzuki, Y.J., Koyaguchi, T., 2013. 3D numerical simulation of volcanic eruption clouds during the 2011 Shinmoe-dake eruptions. *Earth Planets Space* 65(6): 581–589. doi:10.5047/eps.2013.03.009.

Textor, C., Graf, H.-F., Longo, A., Neri, A., Esposti Ongaro, T., Papale, P., Timmreck, C., Ernst, G. G. J., Numerical simulation of explosive volcanic eruptions from the conduit flow to global atmospheric scales. *Annals of Geophys*. 48, 4/5.

Tupper, A., Textor, C., Herzog, M., Graf, H.-F, Richards, M. S., 2009. Tall clouds from small eruptions: the sensitivity of eruption height and fine ash content to tropospheric instability. *Nat. Hazards* 51, 375–401.

Valentine, G. A., Wohletz, K. H., 1989. Numerical models of Plinian eruption columns and pyroclastic flows. *J. Geophys. Res*. 94, 1867–1887.

Van Eaton, A. R., Herzog, M., Wilson, C. J. N., McGregor, J. 2012. Ascent dynamics of large phreatomagmatic eruption clouds: The role of microphysics. *J. Geophys. Res.* 117, B03203. doi: 10.1029/2011JB008892.

Van Eaton, A.R., Mastin, L.G., Herzog, M., Schwaiger, H.-F., Schneider, D. J., Wallace, K. L. W., Clarke, A. B., 2015. Hail formation triggers rapid ash

aggregation in volcanic plumes. *Nature Communications*. doi:10.1038/ncomms8860.

van Leer, B., 1977. Towards the ultimate conservative difference scheme III. Upstream-centered finite-difference schemes for ideal compressible flow. *J. Comput. Phys.* 23, 263–275. doi:10.1016/0021-9991(77)90094-8.

Woods, A. W., 1988. The fluid dynamics and thermodynamics of eruption columns. *Bull. Volcanol.* 50, 169–193.

Woods, A. W., Bursik, M. I., 1991. Particle fallout, thermal disequilibrium and volcanic plumes. *Bull. Volcanol.* 53, 559–570.

Woods, A. W., Self, S., 1992. Thermal disequilibrium at the top of volcanic clouds and its effect on estimates of the column height. *Nature*, 355, 628–630.

FIGURE CAPTIONS

Figure 1. Simulation results by the SK-3D model for the weak plume case. The snapshot of $t = 600$ s after the eruption initiation; (a) isosurface where the mass fraction of the erupted material is 0.002, and the vertical cross-sections of (b) the mass fraction of the erupted material, (c) the density difference relative to the atmospheric density at the same vertical position, (d) the temperature difference relative to the atmospheric temperature at the same vertical position, and (e) the upward velocity.

Figure 2. Simulation results by the SK-3D model for the strong plume case. The snapshot of $t = 900$ s after the eruption initiation; (a) isosurface where the mass fraction of the erupted material is 0.002, and the vertical cross-sections of (b) the mass fraction of the erupted material, (c) the density difference relative to the atmospheric density at the same vertical position, (d) the temperature difference relative to the atmospheric temperature at the same vertical position, and (e) the upward velocity.

Figure 3. Time evolution of the maximum height of the plume based on the simulation results of (a) SK-3D and (b) PDAC for the weak (left) and strong (right) plume cases. The curves are defined by different thresholds of particle concentration with respect to the value at the inlet.

Figure 4. Vertical profiles of the mean mass fraction of the erupted material in the umbrella clouds, integrated from $r > 3$ km for the weak plume case and $r > 30$ km for the strong plume case on the basis of the results of SK-3D (see the arrows in Figs 1b and 2b). The mass fraction (mf_m) is normalized by its peak value ($mf_{m,max}$). The horizontal lines represent the level of maximum radial spreading.

Figure 5. Vertical profiles of the air fraction entrained into the plume which are horizontally integrated from the three dimensional results for the weak (left) and strong (right) plumes for windless case. The profiles illustrated by red and blue points are derived by using the different time windows with the SK-3D model (top) and the PDAC model (bottom). ASHEE shows similar trends in the Strong Plume case.

Figure 6. Vertical cross-sections of the mass fraction of the erupted material in x–z space for the weak plume case without wind effects. Results of (a) ATHAM, (b) SK-3D, (c) ASHEE, and (d) PDAC. The time averaging interval is [600:660s].

Figure 7. Time-averaged, vertical cross-sections of the mass fraction of the erupted material in x–z space for the strong plume in a windless atmosphere. Results of (a) ATHAM, (b) SK-3D, (c) ASHEE, and (d) PDAC. The time averaging interval is [900:960s]. In the simulations of ASHEE and PDAC, the lateral domains are limited to be ~50km from the vent.

Figure 8. Plume heights obtained from the 3D models for (a) weak plume and (b) strong plume cases. Blue, red, and green bars indicate the maximum height, NBL, and spreading level, respectively. The time averaging intervals are [600:660s] for the weak plume case and [900:960s] for the strong plume case. The averages of the 3D and 1D simulation results are also illustrated.

Figure 9. Vertical profiles of physical quantities horizontally integrated from the 3D results for the weak plume for windless case; (a) the air fraction entrained into the plume, (b) the mixture density, (c) the gas fraction, (d) the plume radius, (e) the solid fraction, (f) the plume temperature, and (g) the plume velocity. The time averaging intervals is [600:660s].

Figure 10. Vertical profiles of physical quantities horizontally integrated from the 3D results for the strong plume for windless case; (a) the air fraction entrained into the plume, (b) the mixture density, (c) the gas fraction, (d) the plume radius, (e) the solid fraction, (f) the plume temperature, and (g) the plume velocity. The time averaging interval is [900:960s]. Note that the lateral domains of the ASHEE and PDAC simulations are limited to be ~50 km from the vent.

Figure 11. Vertical profile of radial entrainment coefficient for the weak and strong plume cases on the basis of the 3D simulation results. The time averaging intervals are [600s;660s] for the weak plume case and [900s;960s] for the strong plume case. The large fluctuations in SK-3D results are mainly due the longer time interval used for the simulation outputs (10 sec instead of 1 sec, see Table 2).

Figure 12. Time-averaged, vertical cross-sections of the particle mass fraction in x–z space for (a, b) the weak and (c, d) the strong plume cases wind effects. Results of (a, c) ATHAM and (b, d) SK-3D. The time averaging intervals are [600:660s] for the weak plume case and [900:960s] for the strong plume case.

Figure A1. Vertical grid sizes employed in all the models for the weak (a) and strong (b) plume cases.

Figure B1. Vertical profiles of the physical quantities calculated by the different filters (*f1*, *f3*, *f4*, and *f5*) for the SK-3D simulation results of the weak plumes for windless case; (a) the air fraction entrained into the plume and (b) the mixture temperature.

Table 1. Summary of the three-dimensional models used in the study. Note that the Label numbers 1, 2, 3, and 4 corresponds to 10, 11, 12, and 13 represented in Costa et al. (this issue), respectively.

Label	1	2	3	4
Name	ATHAM[1]	SK-3D[2]	ASHEE[3]	PDAC[4]
LES	Yes	No	Yes	Yes
Components	Air, water, particles	Air, erupted material	Air, water, particles	Air, water, particles
Particle fallout	Yes	No	Yes	Yes
Atmospheric moisture	Yes	No	Yes	No
Water latent heat	Yes	No	Yes	No
Cloud microphysics	Yes	No	No	No

1: Herzog et al. (1998; this issue), 2: Suzuki et al. (2005), Suzuki and Koyaguchi (2009, 2015),

3: Cerminara et al. (2016a), 4: Neri et al. (2003), Esposti Ongaro et al. (2007), Carcano et al. (2013)

Table 2. Summary of the three-dimensional models numerical parameters.

Label	1	2	3	4
Name	ATHAM	SK-3D	ASHEE	PDAC
Numerical method	FDM	FDM	FVM	FVM
Accuracy of scheme	2nd order	3rd order	2nd order	2nd order
Weak Plume case				
Domain size (km³)	30×30×30	14×14×15	$\pi \times 13^2 \times 21$	20×20×20
T_{max} (sec)	1800	710	720	1000
ΔX_{min}	$D_0/3$ (18 m)	$D_0/20$ (3 m)	$D_0/32$ (2 m)	$D_0/3$ (18 m)
ΔX_{max}	600m	$D_0/2$ (27 m)	70m	200m
Δt (sec)	~0.1	~10^{-3}	1.5×10^{-3}	10^{-2}
N_{tot}	15×10^6	170×10^6	11×10^6	8.0×10^6
T_{CPU} (hour)	108	580	520	250
N_{cores}	64	512	1024	62
ΔT_{out}	1 sec	1 sec	every time step	1 sec
Strong Plume case				
Domain size (km³)	350x350x60	300×300×68	$\pi \times 46^2 \times 50$	100×100×60
T_{max} (sec)	3600	1600	2000	1000
ΔX_{min}	$D_0/13$ (109 m)	$D_0/40$ (35 m)	$D_0/32$ (44 m)	$D_0/30$ (47 m)
ΔX_{max}	4 km	300 m	300 m	1 km
Δt (sec)	~0.25	~10^{-2}	2.0×10^{-2}	10^{-2}
N_{tot}	6.3×10^6	300×10^6	8.8×10^6	10×10^6
T_{CPU}	69	160	160	280
N_{cores}	64	384	1024	62
ΔT_{out}	1 sec	10 sec	every time step	1 sec

T_{max}: Maximum simulated time, N_{tot}: Number of discretization elements, T_{CPU}: Total execution

time, N_{cores}: Number of CPU cores utilized, ΔT_{out}: Output interval.

Table 3. Volcanic input parameters for simulations.

Parameter	Weak plume		Strong plume	
Vent elevation	1500 m		1500 m	
Eruption duration	0.2 hours		2.5 hours	
Mass eruption rate	1.5×10^6 kg s^{-1}		1.5×10^9 kg s^{-1}	
Exit velocity	135 m s^{-1}		275 m s^{-1}	
Exit temperature	1273 K		1053 K	
Exit water fraction	3.0 wt%		5.0 wt%	
Particle properties	coarse	fine	coarse	fine
Diameter	1 mm	62.5 μm	0.5 mm	15.6 μm
Density	2200 kg m^{-3}	2700 kg m^{-3}	2500 kg m^{-3}	2700 kg m^{-3}
Mass fraction	48.5 wt%	48.5 wt%	47.5 wt%	47.5 wt%

Table 4. Results for the weak plume case without wind effects. The time averaging intervals are [600:660s]. The mass fraction of 0.01 was used to estimate the plume height.

Model	Height (km)	NBL (km)	Spreading level (km)
ATHAM	16.1	5.7	7.2
SK-3D	11.1	6.9	7.9
ASHEE	10.4	6.8	8.2
PDAC	11.0	7.9	9.0
Average	12.1	6.8	8.1
SD	2.7	0.9	0.7
SD %	22.0	13.2	9.0
Average(1D)	9.0	6.7	-

Table 5. Results for the strong plume case without wind effects. The time averaging

intervals are [900:960s]. The mass fraction of 0.01 was used to estimate the plume

height.

Model	Height (km)	NBL (km)	Spreading level (km)
ATHAM	33.4	16.2	18.1
SK-3D	39.9	20.0	29.8
ASHEE	36.7	22.1	24.0
PDAC	42.5	28.5	31.0
Average	38.1	21.7	25.7
SD	3.9	5.1	5.9
SD %	10.4	23.7	23.0
Average(1D)	38.8	25.3	-

Table 6. Column heights for windy case. The time averaging intervals are [600:660s] for the weak plume case and [900:960s] for the strong plume case. The mass fraction of 0.01 was used to estimate the plume height.

Model	Weak plume Height (km)	NBL (km)	Strong plume Height (km)	NBL (km)
ATHAM	5.5	3.8	32.0	15.7
SK-3D	6.5	3.5	39.9	17.9
Average(1D)	4.0	3.2	32.0	23.5

Figure 1

(a) 3D bird view

(b) Mass fraction of erupted material

(c) Density difference

(d) Temperature difference

(e) Upward velocity
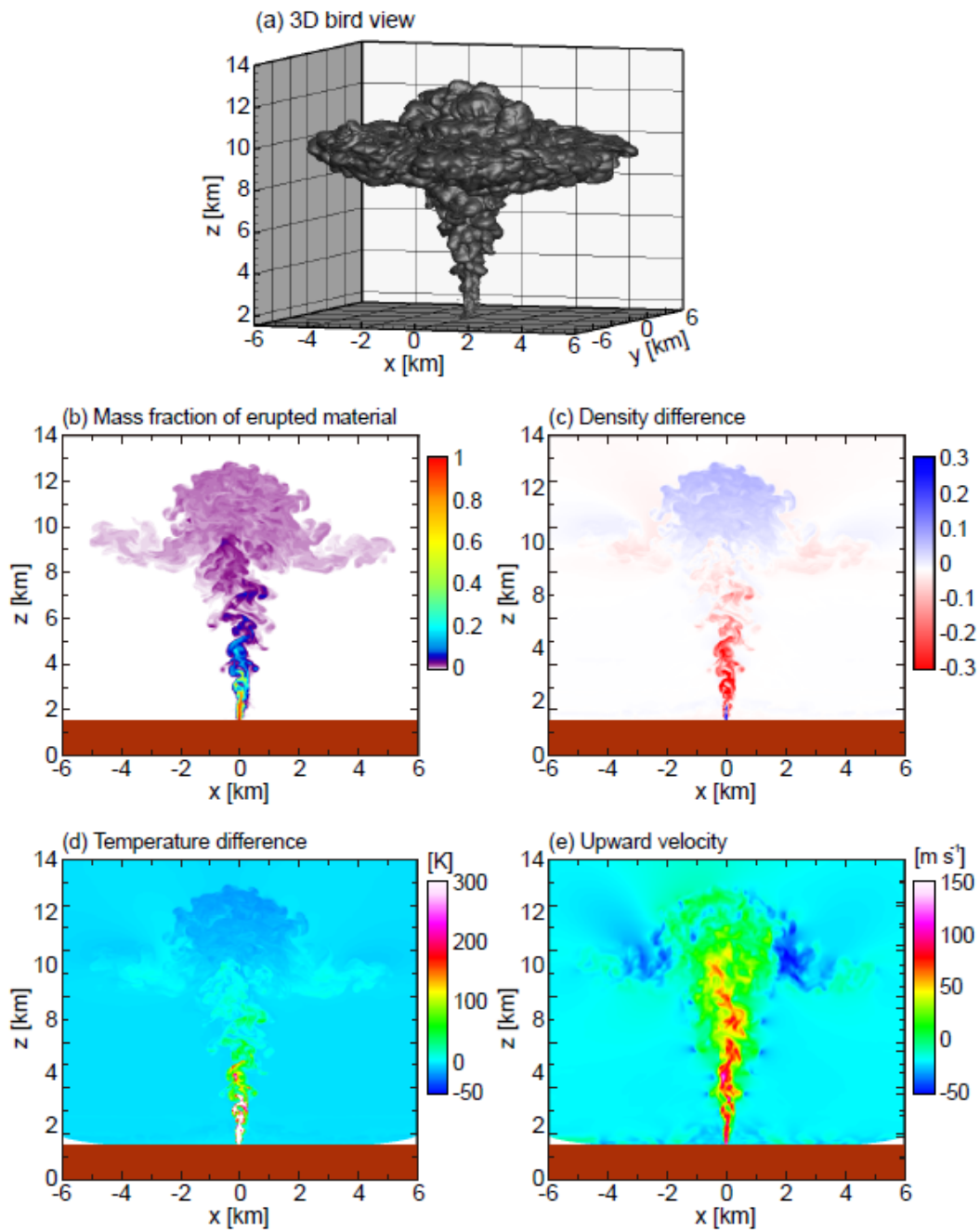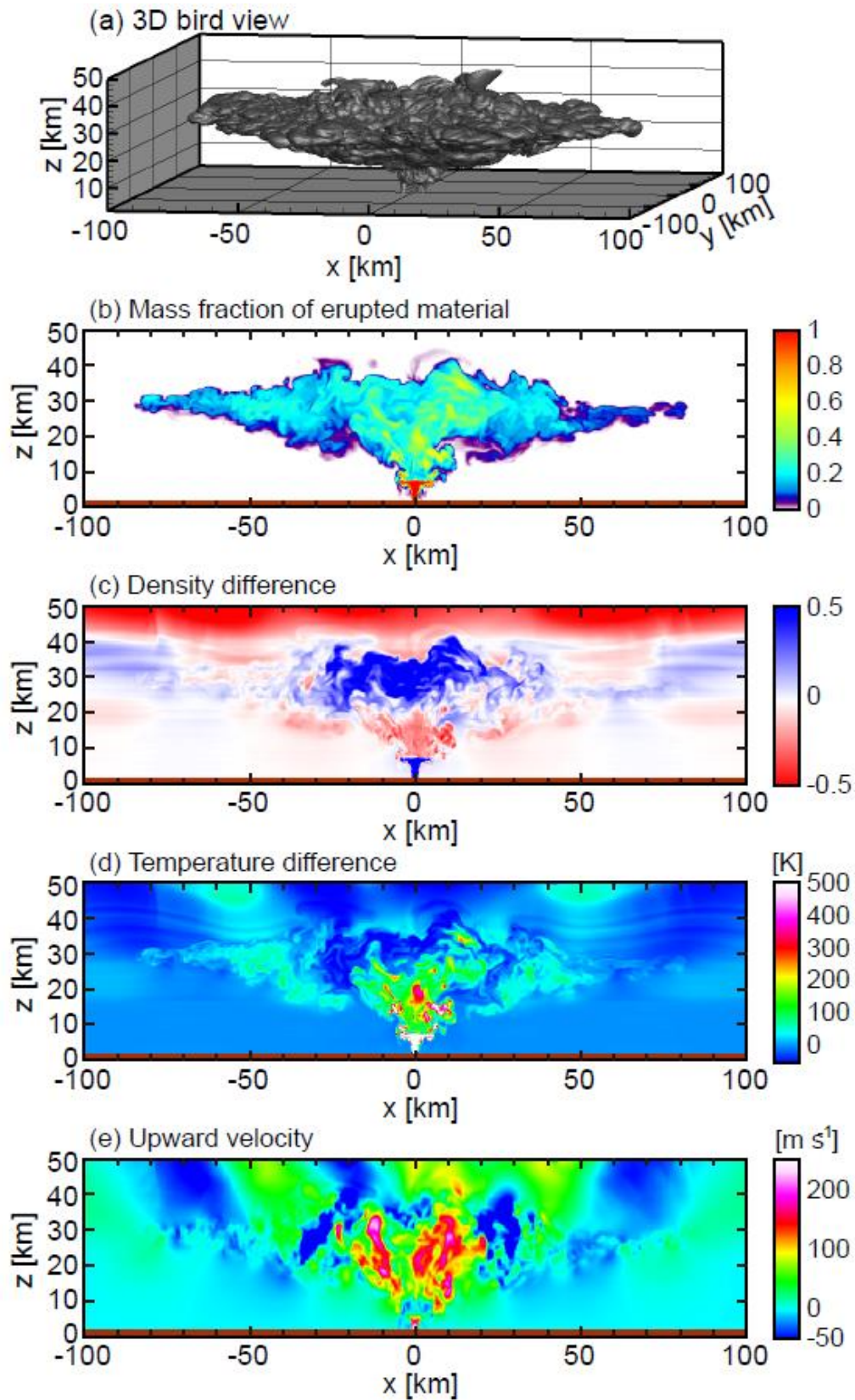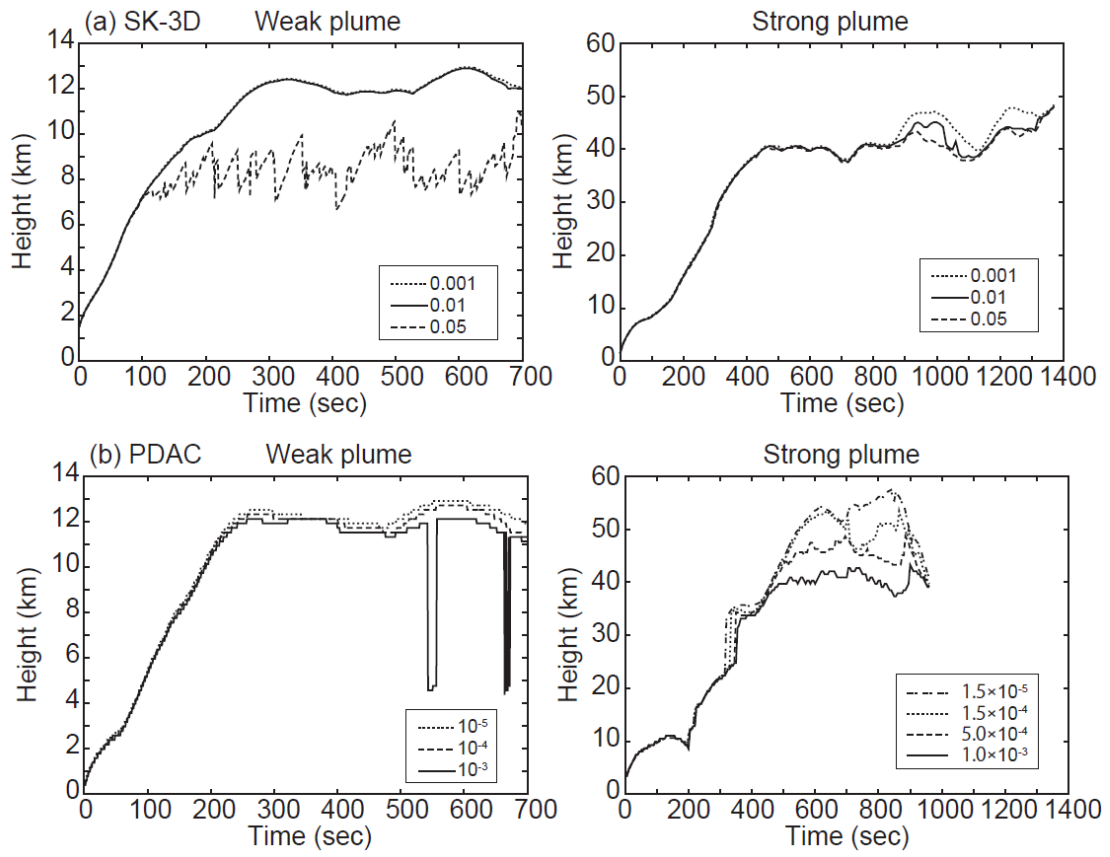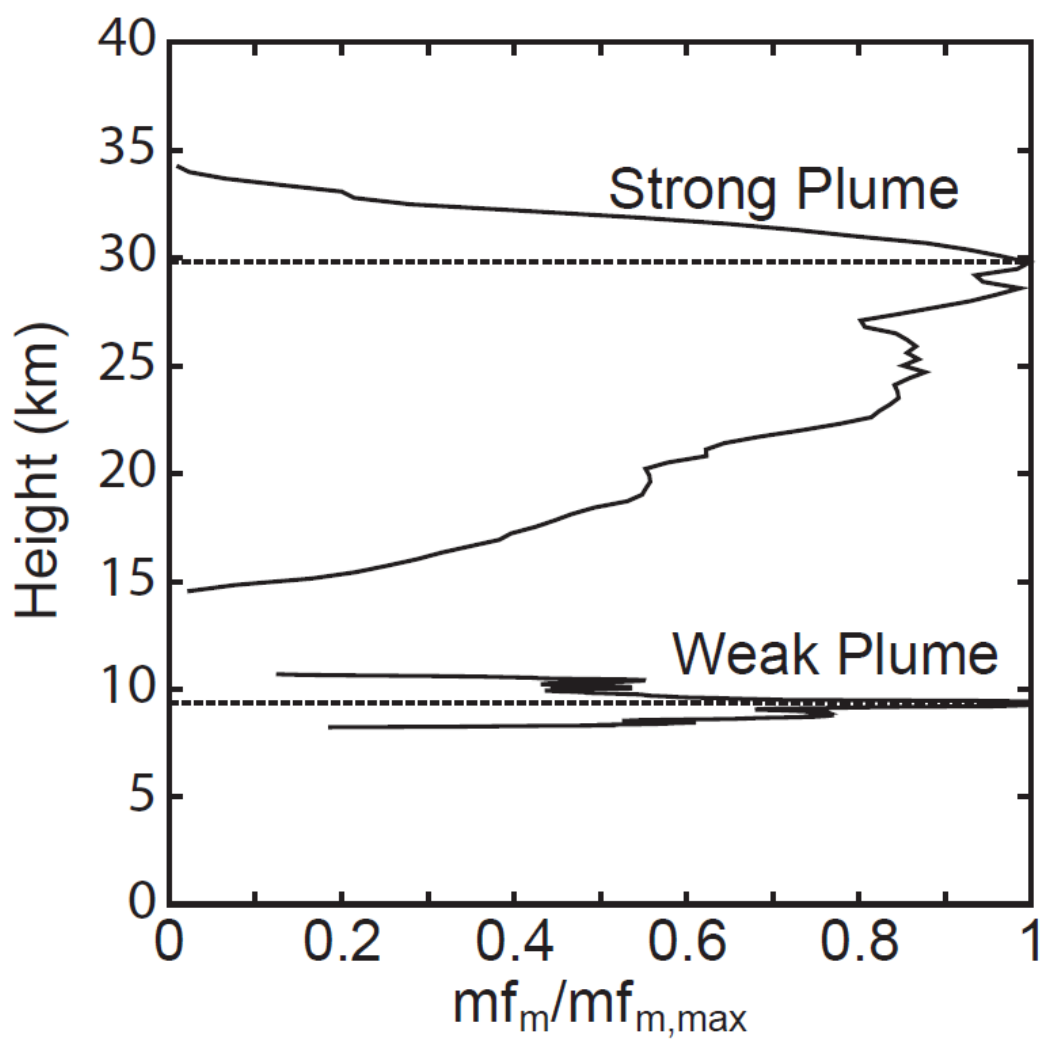
Figure 2

Figure 3

Figure 4
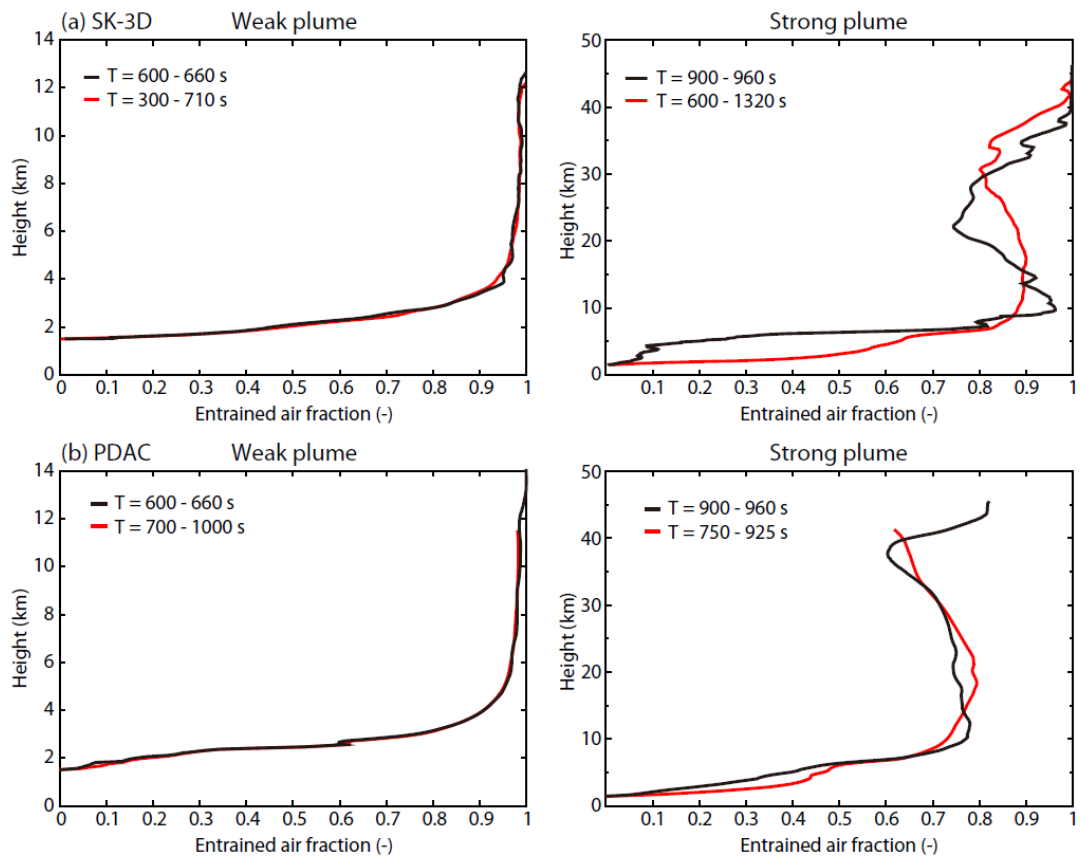
Figure 5
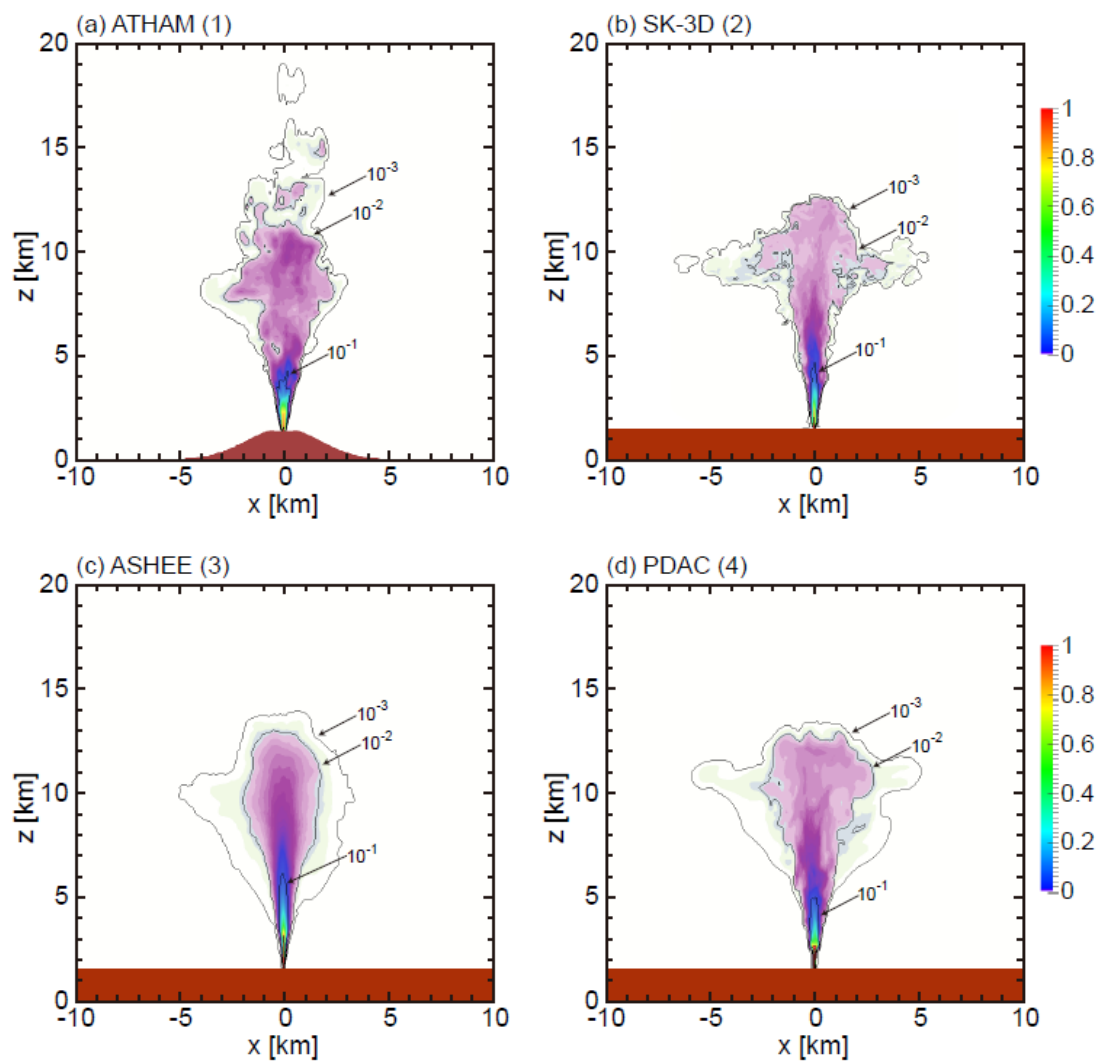
Figure 6
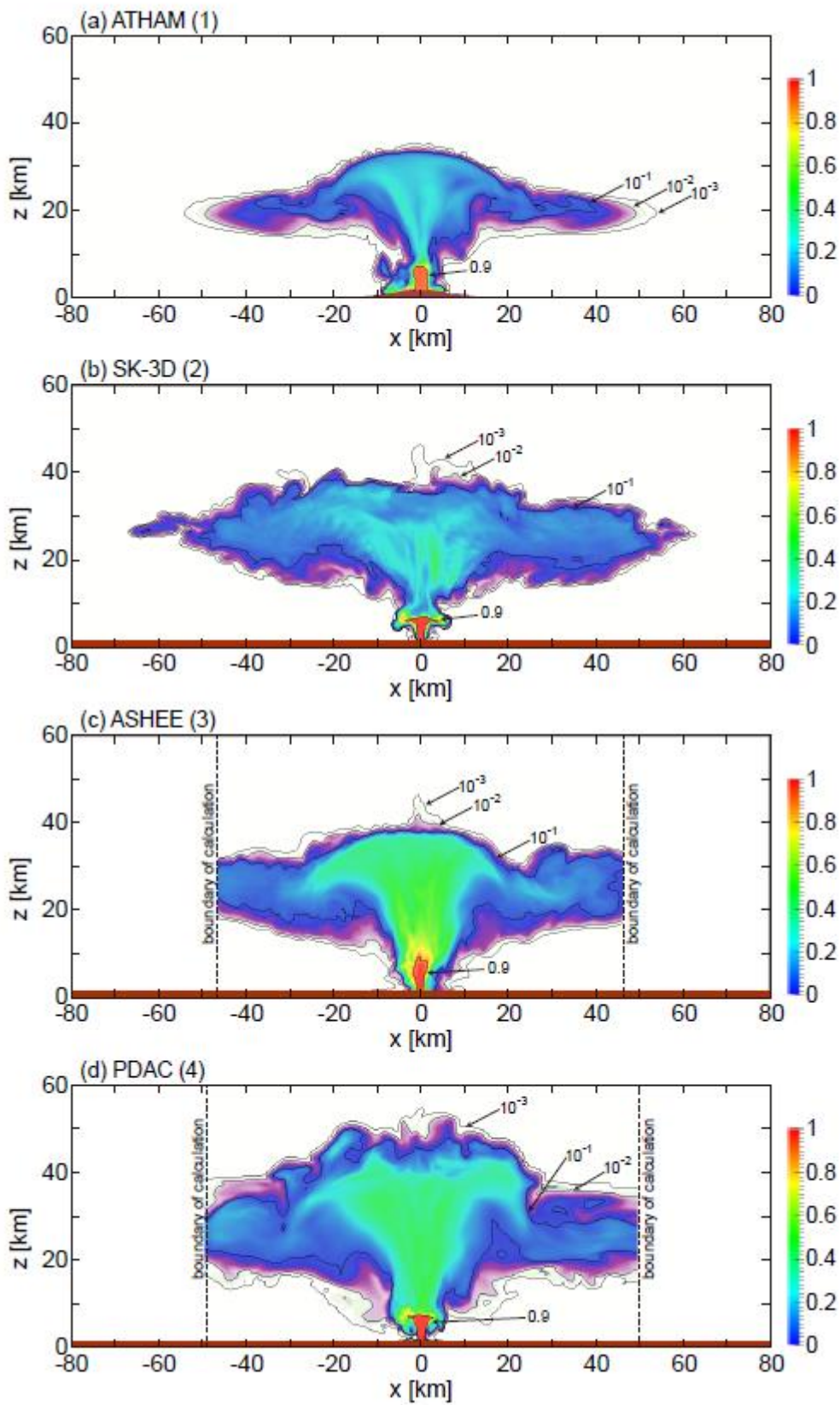
Figure 7
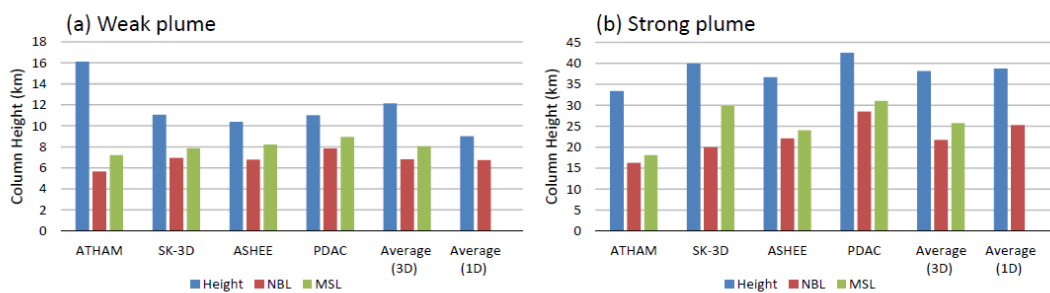
Figure 8
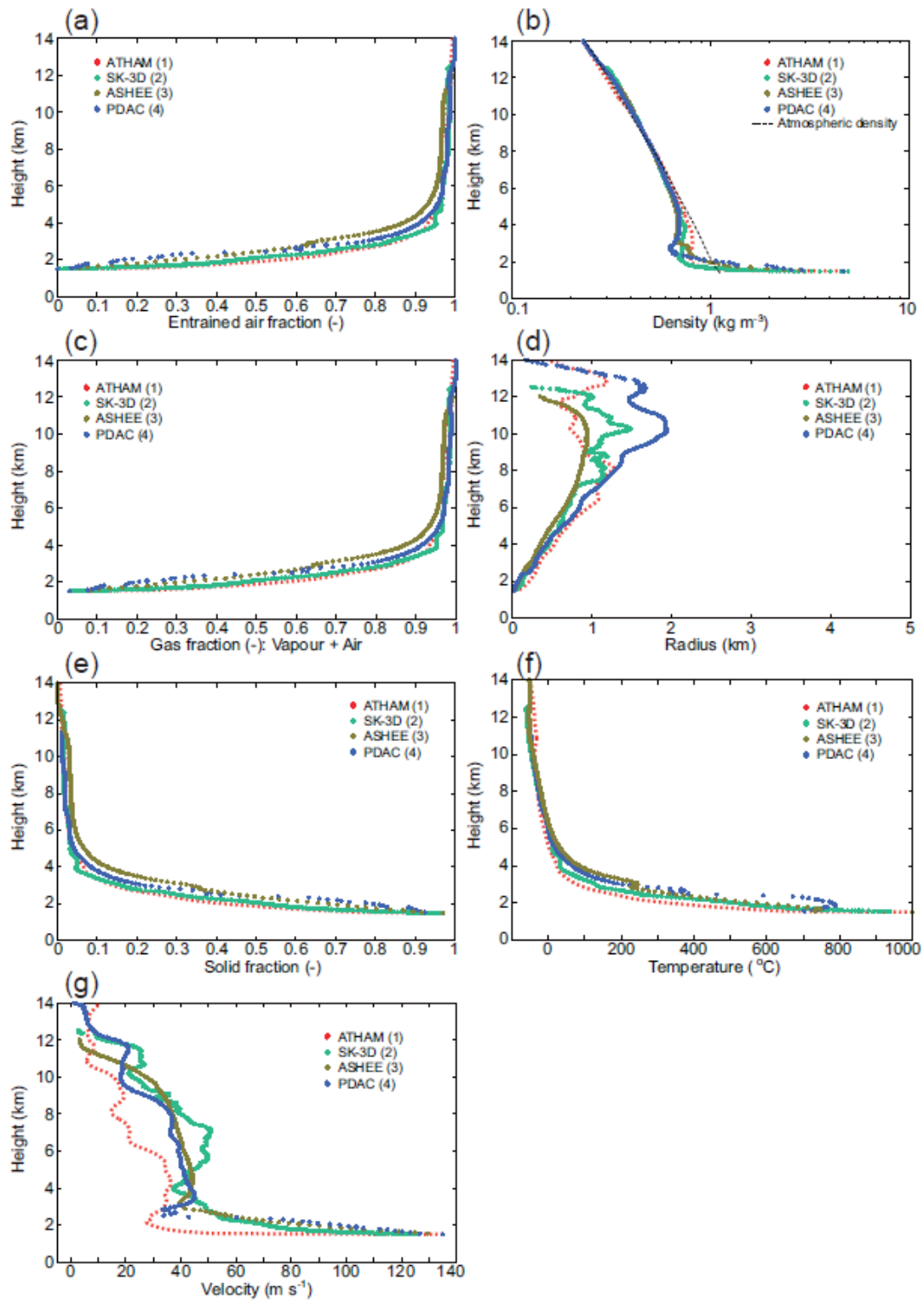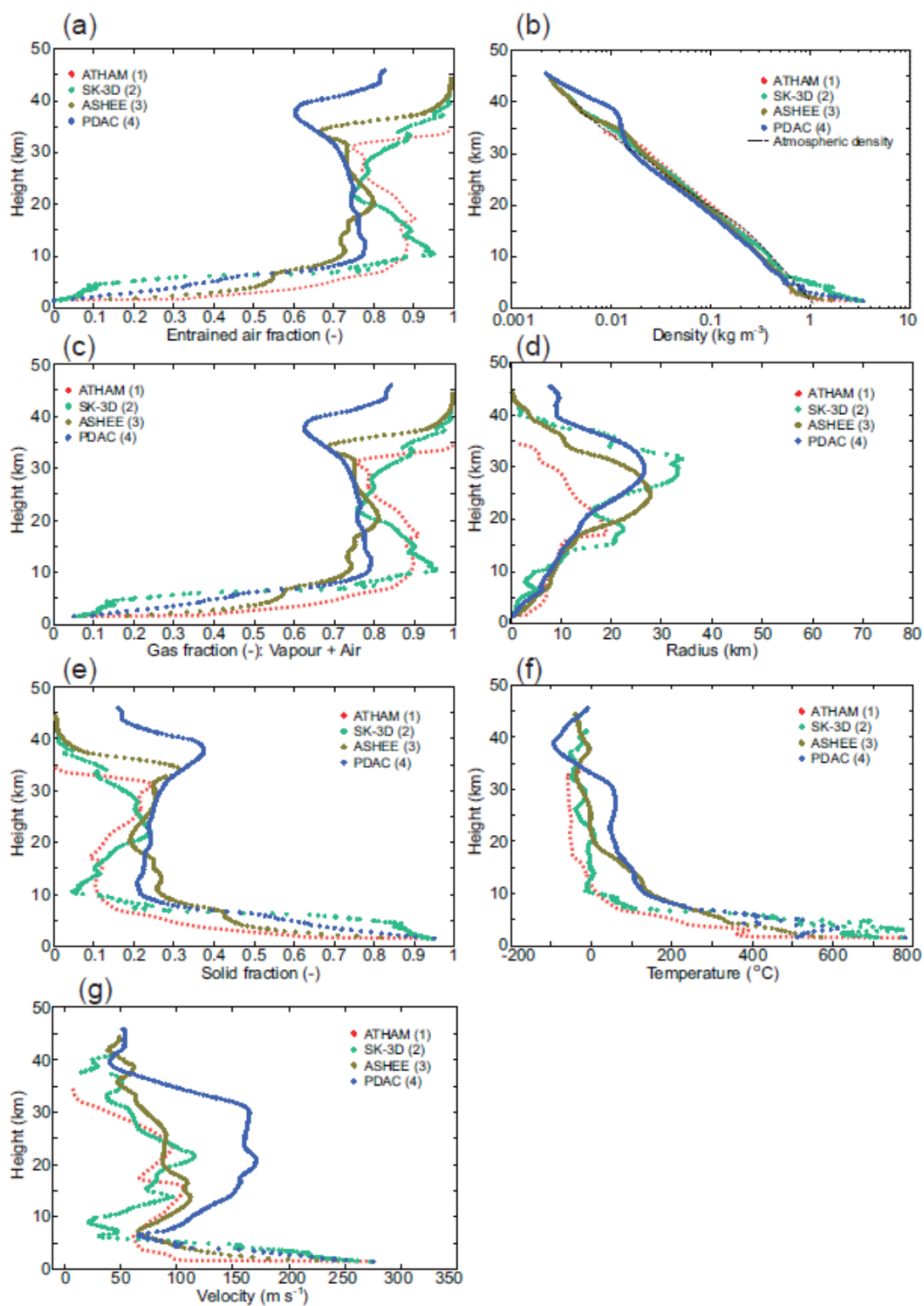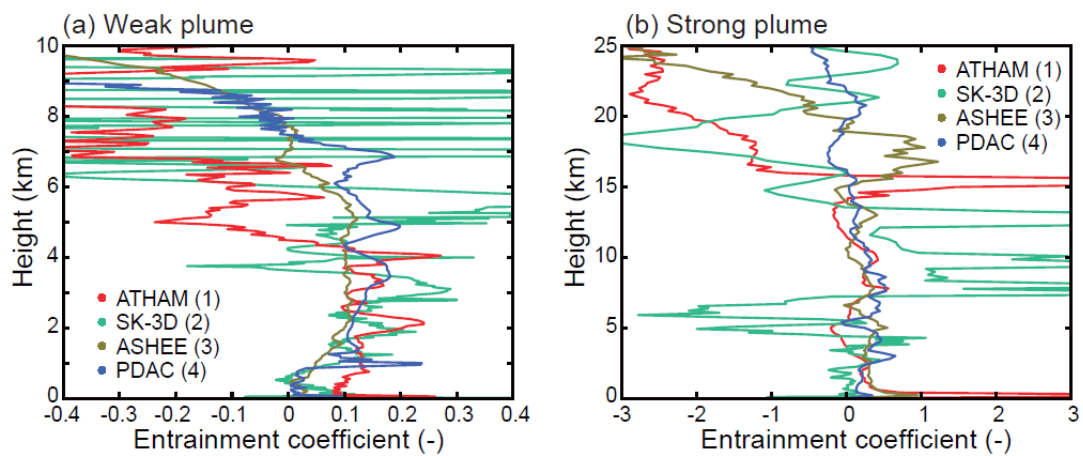
Figure 9

Figure 10

Figure 11
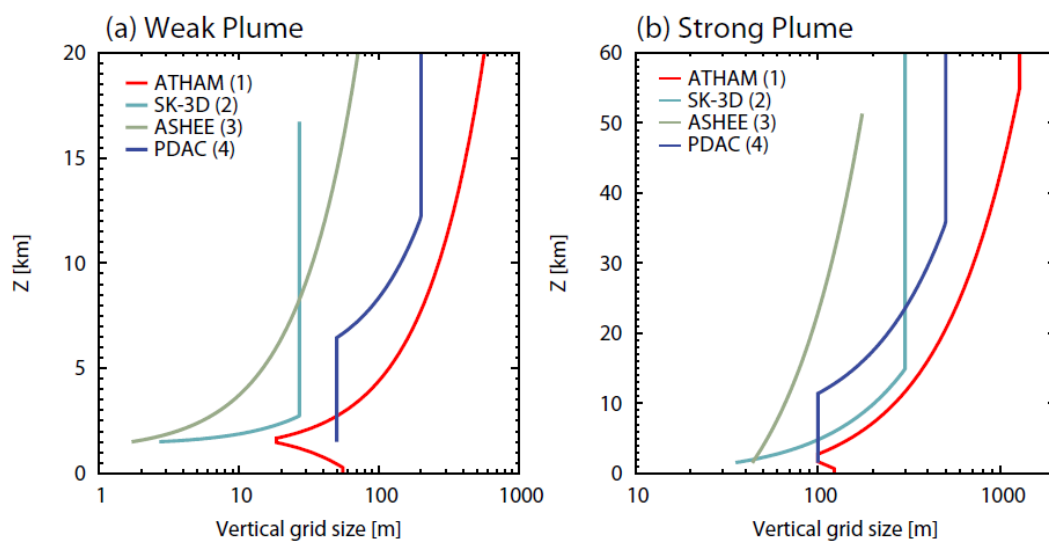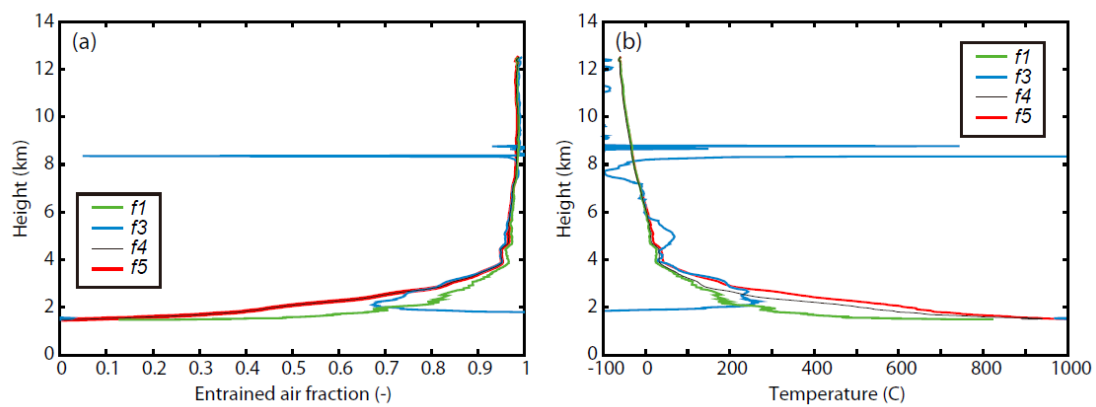
Figure 1A

Figure B1

Highlights

- We performed an inter-comparison study of three-dimensional models of volcanic plumes.

- Simulations with common input parameters for a weak and strong eruption columns were carried out.

- Although the models use different numerical procedures, the qualitatively consistent results were obtained among the models.

- We discussed the possible sources of diversity among the results obtained from the different model.